

## Laboratory 19

# Quantitative Energy-Dispersive X-Ray Microanalysis

### 19.1 Operating Conditions for EDS Analysis

**Experiment 19.1: Measurement of X-Ray Intensities.** Figures A19.1 through A19.3 show EDS spectra from the NiCrAl specimen at 10, 15, and 30 kV, respectively. The take-off angle is 42.0° with the specimen tilted at 30.0° and the x-ray detector at a 12.0° take-off angle (when the specimen tilt was 0°).

Tables A19.1-A19.3 summarize the data obtained from the nickel, chromium, and aluminum standards as well as the analyses of the NiCrAl sample at each of the operating voltages, 10, 15, and 30 kV. Values of  $N$ ,  $N_B$ , and  $N_P$  are listed in the tables. The net intensity values  $N_P$  were obtained by using a fit of the continuum background (for  $N_B$ ) and subtracting this background from the peak intensities  $N$ .

Calculated values of the relative counting error (RCE) are also given in Tables A19.1-A19.3. The RCE is below 1.1% for nickel and chromium at all voltages. However, the relative counting error for Al increases with voltage from ~0.81% at 10 kV to ~1.46% at 15 kV to ~2.2% at 30 kV. Errors in the compositional analysis greater than the RCE are due to factors other than the counting uncertainties of each measurement.

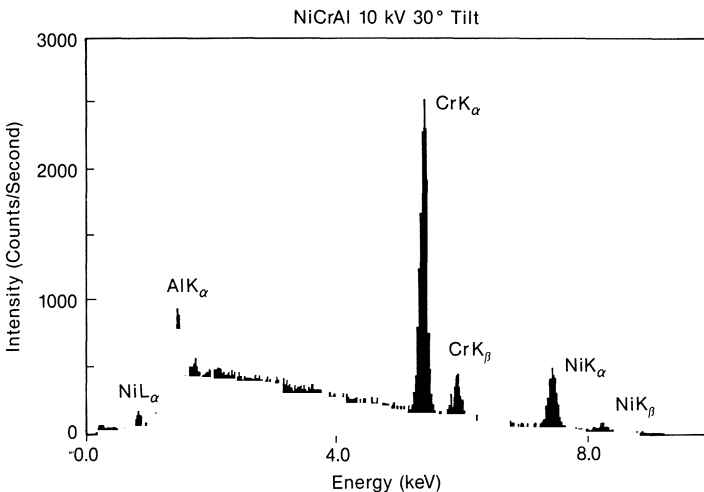


**Figure A19.1.** EDS spectrum of NiCrAl collected at 10 kV.

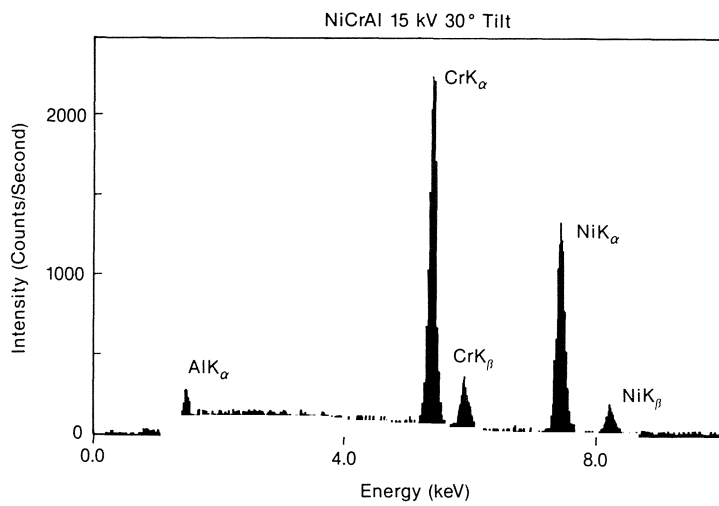


**Figure A19.2.** EDS spectrum of NiCrAl collected at 15 kV.

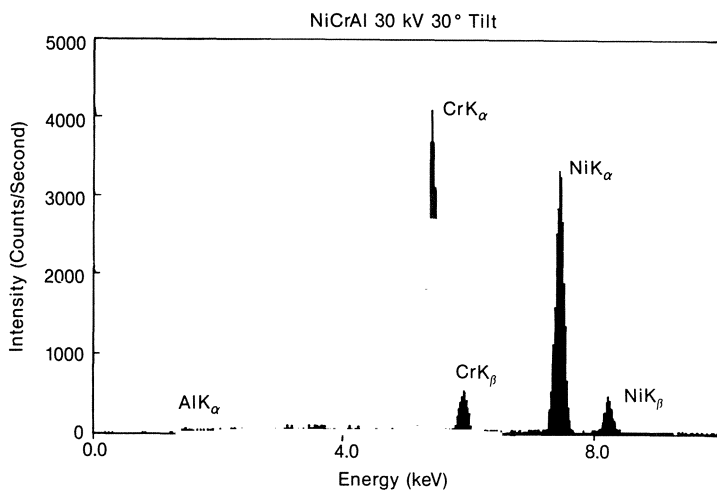


**Figure A19.3.** EDS spectrum of NiCrAl collected at 30 kV.

**Table A19.1** 10-kV NiCrAl Results by EDS**10 kV, 100 sec live time**

<b>Standards</b>	<b><i>N</i></b>	<b><i>N<sub>B</sub></i></b>	<b><i>N<sub>P</sub></i></b>				
$\text{Ni}K_{\alpha}$	11,116	1,482	9,634				
$\text{Cr}K_{\alpha}$	71,804	3,170	68,634				
$\text{Al}K_{\alpha}$	229,880	4,122	225,758				
<b>X-ray line</b>	<b><i>N</i></b>	<b><i>N<sub>B</sub></i></b>	<b><i>N<sub>P</sub></i></b>	<b>RCE (%)</b>	<b><i>K</i> ratio</b>	<b>Meas. wt(%)</b>	<b>% Rel. error</b>
$\text{Ni}K_{\alpha}$	6,882	1,263	5,619	1.09	0.5670	57.10	-2.45
$\text{Cr}K_{\alpha}$	29,879	3,142	26,737	0.547	0.3920	39.00	1.28
$\text{Al}K_{\alpha}$	9,569	3,514	6,055	0.813	0.0233	3.21	6.54
$\text{Ni}K_{\alpha}$	6,827	1,427	5,400	1.08	0.5610	56.50	-3.50
$\text{Cr}K_{\alpha}$	29,813	3,081	26,732	0.548	0.3870	38.50	0
$\text{Al}K_{\alpha}$	9,615	3,466	6,149	0.816	0.0228	3.14	4.46
$\text{Ni}K_{\alpha}$	6,772	1,401	5,371	1.08	0.5460	55.00	-6.36
$\text{Cr}K_{\alpha}$	30,362	2,998	27,364	0.548	0.3950	39.40	2.28
$\text{Al}K_{\alpha}$	9,724	3,514	6,210	0.810	0.0237	3.25	7.69
$\text{Ni}K_{\alpha}$	6,992	1,375	5,617	1.07	0.5870	59.10	1.02
$\text{Cr}K_{\alpha}$	30,156	3,141	27,015	0.545	0.3960	39.30	2.03
$\text{Al}K_{\alpha}$	9,556	3,508	6,048	0.814	0.0226	3.11	3.54
Ave Ni			5,502	1.08	0.5710	57.50	-1.74
Ave Cr			26,962	0.547	0.3930	39.10	1.53
Ave Al			6,116	0.815	0.0230	3.17	5.36

**Table A19.2** 15-kV NiCrAl Results by EDS

**15 kV, 100 sec live time**

Standards	N	N <sub>B</sub>	N <sub>P</sub>	RCE (%)	K ratio	Meas. wt(%)	% Rel. error
NiK <sub>α</sub>	30,901	1,017	29,884				
CrK <sub>α</sub>	68,264	1,773	66,491				
AlK <sub>α</sub>	109,367	1,588	107,779				
 X-ray line	 N	 N <sub>B</sub>	 N <sub>P</sub>	 RCE (%)	 K ratio	 Meas. wt(%)	 % Rel. error
NiK <sub>α</sub>	17,635	938	16,697	0.733	0.5610	57.30	-2.09
CiK <sub>α</sub>	27,721	1,446	26,275	0.585	0.3930	38.40	-0.26
AlK <sub>α</sub>	2,864	1,114	1,750	1.460	0.0150	3.19	5.96
NiK <sub>α</sub>	17,791	910	16,881	0.730	0.5690	58.10	-0.69
CrK <sub>α</sub>	27,606	1,567	26,039	0.585	0.3890	38.00	-1.32
AlK <sub>α</sub>	2,899	1,171	1,728	1.430	0.0155	3.30	9.09
NiK <sub>α</sub>	17,848	953	16,894	0.728	0.5630	57.50	-1.74
CrK <sub>α</sub>	27,459	1,478	25,981	0.587	0.3880	37.90	-1.58
AlK <sub>α</sub>	2,804	1,088	1,716	1.480	0.0147	3.13	4.15
Ave Ni			16,824	0.733	0.5630	57.60	-1.56
Ave Cr			26,098	0.585	0.3930	38.20	-0.79
Ave Al			1,731	1.460	0.0160	3.20	6.30

**Table A19.3** 30-kV NiCrAl Results by EDS

**30 kV, 100 sec live time**

Standards	<i>N</i>	<i>N<sub>B</sub></i>	<i>N<sub>P</sub></i>				
X-ray line	<i>N</i>	<i>N<sub>B</sub></i>	<i>N<sub>P</sub></i>	RCE (%)	<i>K</i> ratio	Meas. wt(%)	% Rel. error
Ni <i>K<sub>α</sub></i>	79,795	1,214	78,581				
Cr <i>K<sub>α</sub></i>	117,252	1,888	115,364				
Al <i>K<sub>α</sub></i>	93,236	1,188	92,048				
Ni <i>K<sub>α</sub></i>	43,903	1,026	42,877	0.47	0.5430	59.30	1.35
Cr <i>K<sub>α</sub></i>	47,915	1,279	46,636	0.45	0.4000	38.90	1.03
Al <i>K<sub>α</sub></i>	1,078	464	614	2.30	0.0062	2.93	-2.39
Ni <i>K<sub>α</sub></i>	43,910	1,099	42,811	0.47	0.5490	60.00	2.50
Cr <i>K<sub>α</sub></i>	48,012	1,345	46,667	0.45	0.4000	38.90	1.03
Al <i>K<sub>α</sub></i>	1,157	530	627	2.16	0.0067	3.16	5.10
Ni <i>K<sub>α</sub></i>	43,893	1,066	42,827	0.47	0.5460	59.70	2.00
Cr <i>K<sub>α</sub></i>	48,349	1,353	46,996	0.45	0.4070	39.50	2.53
Al <i>K<sub>α</sub></i>	1,126	571	555	2.09	0.0064	3.02	0.66
Ni <i>K<sub>α</sub></i>	43,697	1,053	42,643	0.47	0.5400	59.00	0.85
Cr <i>K<sub>α</sub></i>	48,374	1,304	47,070	0.45	0.4050	39.40	2.53
Al <i>K<sub>α</sub></i>	1,157	504	653	2.21	0.0065	3.06	1.96
Ave Ni			42,681	0.47	0.5430	59.30	1.35
Ave Cr			46,766	0.45	0.4050	39.20	2.53
Ave Al			604	2.20	0.0066	3.10	3.20

**Table A19.4** ZAF Analysis for 15 kV and a 42° Take-Off Angle

X-ray line	K ratio	Z	A	F	ZAF	Conc (wt%)
NiK <sub>α</sub>	0.561	0.998	1.02	1.000	1.02	57.3
CrK <sub>α</sub>	0.393	1.010	1.01	0.954	0.97	638.4
AlK <sub>α</sub>	0.015	0.918	2.37	1.000	2.13	3.20
						98.9

## 19.2 Calculation of Composition

**Experiment 19.2: ZAF Correction of Intensities.** (a) A ZAF quantitative analysis procedure was used to convert the intensity ratio (*K* ratio) for nickel, chromium, and aluminum at each point to concentration values. The ZAF correction procedure includes the absorption (*A*) correction of Philibert, the atomic number (*Z*) correction of Duncumb/Reed, which utilizes the mean ionization potentials of Berger/Seltzer and the backscatter correction of Heinrich, and the fluorescence (*F*) correction of Reed.

A ZAF calculation performed at 15 kV and at a 42.0° take-off angle for the first data point at 15 kV from the NiCrAl alloy is shown in Table A19.4. For the 15-kV ZAF correction, the chromium concentration is adjusted only +1.3% relative to the *K* ratio and the nickel concentration is adjusted only +2.1% relative to the *K* ratio. However, the absorption correction factor for aluminum is 2.37 and the total ZAF correction of 2.13 leads to a major adjustment in the *K* ratio of aluminum by almost +100%. Clearly any major ZAF calculation error would occur in the aluminum concentration due to the large absorption correction. At 10 kV the ZAF correction for aluminum is less, 1.40, and at 30 kV the ZAF correction for aluminum is much greater, 4.7.

(b) Tables A19.1-A19.3 also include the calculated composition for each data point at each voltage as well as a listing of the percent of relative error [Equation (19.5)].

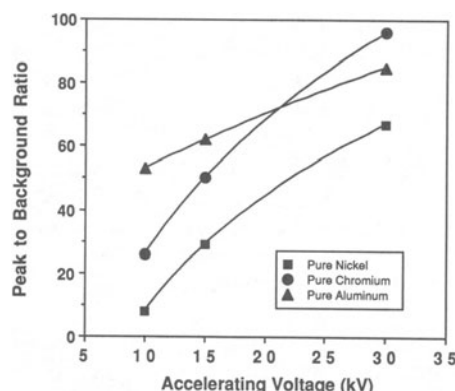


**Figure A19.4.** EDS peak-to-background ( $N_T/N_B$ ) variation with voltage for pure elements.

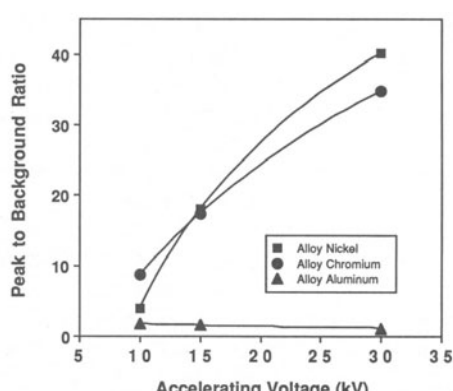


**Figure A19.5.** EDS peak-to-background ( $N_T/N_B$ ) variation with voltage for NiCrAl alloy.

**Table A19.5 ZAF Summary of NiCrAl Data**

Element	Known composition (wt%)	10 kV		15 kV		30 kV	
		Conc. (wt%)	Rel.error (%)	Conc. (wt%)	Rel.error (%)	Conc. (wt%)	Rel.error (%)
Ni	58.5	57.5	-1.74	57.6	-1.56	59.3	+1.35
Cr	38.5	39.1	+1.53	38.2	-0.79	39.5	-2.53
Al	3.0	3.17	+5.36	3.2	+6.30	3.1	+3.20
Total	100.0	99.8		99.0		101.9	

(c) Figure A19.4 shows the variation of  $P/B$  of nickel, chromium, and aluminum with voltage for the three pure element standards. The companion Figure A19.5 shows the variation of  $P/B$  with voltage for the same elements in the NiCrAl alloy.

Table A19.5 summarizes the average composition of the NiCrAl alloy obtained by multiple analyses at each voltage. The table also includes the calculated percent relative error for each composition measurement. The measured concentrations of the NiCrAl add up closely to 100%.

#### Questions:

1. The relative error in the determination of aluminum in the NiCrAl alloy is 3.5%-7.7% rel at 10 kV, 4.1%-9.1% rel at 15 kV, and -2.4%-5.1% rel at 30 kV as given in Tables A19.1-A19.3. The 10- and 15-kV data are always slightly over-corrected by the ZAF technique. The maximum range of the percent relative error is encountered at 30 kV where, because of very high absorption, the largest correction in the  $K$  ratio is made.

2. The relative error (percent) for chromium does not vary in any regular way with voltage and rarely exceed 2.5%. The analytical errors for nickel are somewhat higher at the low 10-kV operating voltage than at 15 and 30 kV (see Tables A19.1-A19.3). This higher relative error is most likely due to counting statistics from the low number of nickel counts measured (~5,500 at 10 kV versus 42,500 at 30 kV) in 100 sec. The ZAF corrections to the  $K$  ratios are much less than 10% even at 30 kV and are not a major cause of analytical errors. Most of the relative errors are probably due to experimental problems such as the reproducibility of the specimen height, the low  $\text{Ni}K_{\alpha}$  count rates when  $U < 2.0$  and beam current drift. The latter problem is most serious in SEM instruments where stabilization of the beam current is not usually available.

3. The relative counting errors for chromium and nickel decrease with increasing voltage, from 0.55 to 0.45 for chromium and from 1.08 to 0.47 to nickel. This improvement of RCE with voltage occurs because the chromium, and most significantly the nickel, counting rate increases with voltage. The major factor which causes the increase in the chromium and nickel counting rate is that the production of  $K_{\alpha}$  radiation increases with voltage relative to the background (see Figures A19.1-A19.3).

4. X-ray intensities varied over 10% relative if the specimen was not brought to the same height. This level of variation precludes quantitative analysis in the SEM. The major reason for the lack of reproducibility is that the EDS detector behind the collimator intercepts a different fraction of x-rays emitted from the sample when the height of the sample is changed. In the SEM instrument used here, the only way to obtain a reproducible sample height, which minimized variations in measured x-ray intensity, was to lock the objective lens focus at one

point and move the specimen vertically with the z-control until the specimen image was in focus. A magnification of 1000x or higher was ideal to use for focusing purposes.

5. Other factors which influence quantitative results are constancy of take-off angle and beam current. In many SEM instruments there is no long-term stability of the electron probe current. Reproducibility is worsened if different samples and standards cannot be analyzed without turning off the current to admit the specimen to the vacuum chamber of the instrument.

6. Using Tables A19.1-A19.3, one can determine how the measured nickel, chromium, and aluminum concentrations vary as a function of position for each voltage measured. The compositional variation and the relative variation in percent are given in Table A19.6. A simplified criterion that has been used to establish the homogeneity of a sample is that if all the data points fall within  $\pm 3 \times \text{RCE}(\%)$  of the average composition, the sample may be considered homogeneous (*SEM XM*, p. 432). The  $\pm 3 \times \text{RCE}(\%)$  homogeneity criteria for each element and voltage were calculated and are listed in Table A19.6. At 30 kV the range of composition lies within or just outside the homogeneity criteria of  $3 \times \text{RCE}$  and the sample would be considered homogeneous. At 10 and 15 kV the range of compositional variation lies within the homogeneity criteria except for the nickel which is clearly outside. The nickel intensities are relatively low particularly at 10 kV (see question 3), which degrades the counting statistics. In addition variations in peak heights from position to position are more difficult to deal with without light optics (question 4) and lead to variations in counting rates. Also, as discussed in question 5, there are the problems of constancy of take-off angle and beam current. It is probable that the  $3 \times \text{RCE}(\%)$  criterion is too strict to establish the homogeneity of a sample using EDS. It is clear the NiCrAl standard is homogeneous if one examines the WDS data obtained in Laboratory 18 for the same sample.

7. As shown in Figure A19.4, the  $P/B$  ratio increases with voltage as expected from the predicted variation of x-ray generation with kV (*SEM XM*, pp. 106-107). However, the  $P/B$  for  $\text{AlK}_\alpha$  decreases with increasing voltage in the NiCrAl specimen (Figure A19.5). It is clear that some improvement in peak-to-background occurs for nickel and chromium, but it is questionable for aluminum in NiCrAl when the overvoltage exceeds 20. Furthermore, the increased absorption effects are clearly undesirable for quantitative calculations. The peak-to-background ratios for nickel, chromium, and aluminum in the standards and in the NiCrAl alloy are much superior using WDS (Figures A18.1-A18.2) than EDS (Figures A19.4-A19.5).

**Table A19.6 Homogeneity Variation**

	Average composition (wt%)	Composition variation (wt%)	Relative variation (%)	$3 \times \text{RCE} (\%)$
<b>10 kV</b>				
Ni	57.5	55.0-59.1	$\pm 4.30$	$\pm 3.24$
Cr	39.1	38.5-39.4	$\pm 1.53$	$\pm 1.64$
Al	3.17	3.11-3.25	$\pm 2.40$	$\pm 2.45$
<b>15 kV</b>				
Ni	57.6	57.3-58.1	$\pm 8.70$	$\pm 2.20$
Cr	38.2	37.9-38.4	$\pm 0.79$	$\pm 1.75$
Al	3.20	3.13-3.30	$\pm 3.10$	$\pm 4.40$
<b>30 kV</b>				
Ni	59.3	58.6-60.0	$\pm 1.18$	$\pm 1.41$
Cr	39.2	38.6-39.5	$\pm 1.53$	$\pm 1.35$
Al	3.10	2.93-3.16	$\pm 5.50$	$\pm 6.60$

**Table A19.7** Comparison of ZAF and  $\phi(\rho z)$  techniques

Element	(ZAF) factor	Comp. (wt%)	$\phi(\rho z)$ factor	Comp. (wt%)
Ni	0.995	39.3	0.999	39.5
Cr	1.008	59.1	1.004	58.9
Al	1.378	3.11	1.347	3.04

**Optional Experiment.** A comparison is made between the ZAF and the  $\phi(\rho z)$  calculation scheme for the 10 kV measured  $K$  ratio results, point 4.

The calculated results were very similar, within 2.2% rel for aluminum, 1.4% rel for chromium, and 0.5% rel for nickel.

The use of a "standardless" calculation technique led to inaccurate compositional values. For example, at 10 kV the results were 3.65 wt% Al, 64.1 wt% Cr, and 32.3% Ni, and at 30 kV the results were 4.23 wt% Al, 37.9 wt% Cr, and 57.9 wt% Ni (compare with Table A19.5). Thus, errors of over 50% rel are possible with the "standardless" procedure. For specimen elements that have x-ray lines which differ widely in energy, such "standardless" techniques often provide incorrect compositions.

### 19.3 Comparing "Standardless Analysis" with Quantitative Analysis Using Standards

**Experiment 19.3: Silicate Analysis.** The raw spectra for the silicate analyses (performed at 15 kV with a take-off angle of 40°) are shown in Figures A19.6-A19.13. The irregular shapes (non-Gaussian) of the Mg, Al, and Si $K_{\alpha}$  peaks and the complicated, nonlinear background are obvious as is the overlap of these peaks. In this experiment, the energy of the Mg $K_{\alpha}$  peak was measured at 1 eV higher than its real value and the measured Al $K_{\alpha}$  and Si $K_{\alpha}$  were 2 eV too high. The gain was *not* recalibrated.

Analysis results using (1) a full quantitative program employing the MgO, Al<sub>2</sub>O<sub>3</sub>, and SiO<sub>2</sub> standard spectra, (2) a semi-"standardless" program employing standard spectra collected by the manufacturer on his SEM, and (3) a "standardless" program employing Gaussian peak shape estimates for the various elements are shown in Table A19.8. As can be seen, the results differ considerably, with the best results obtained for the full quantitative procedure (error < 0.1% for MgSiO<sub>3</sub>) and the worst result for the completely standardless procedure. Thus, using the full quantitative procedure employing standards, one can obtain accuracy as good as that obtained with WDS techniques.

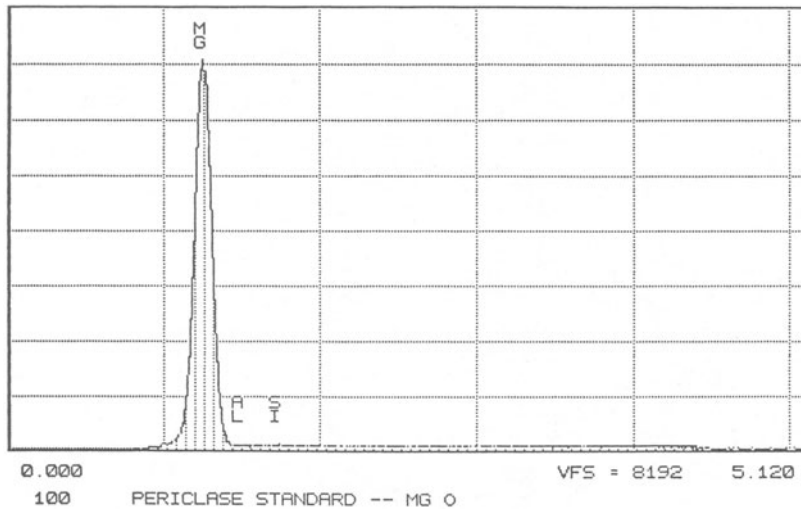


**Figure A19.6.** Magnesium reference peak from MgO standard.

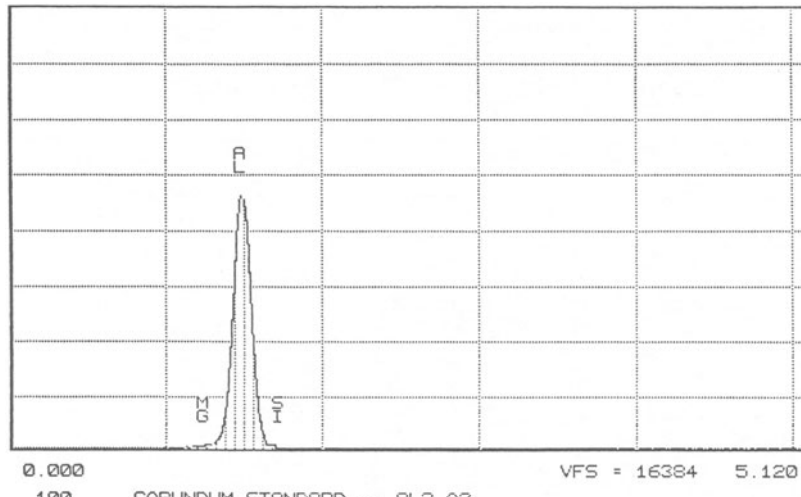


**Figure A19.7.** Aluminum reference peak from Al<sub>2</sub>O<sub>3</sub> standard.

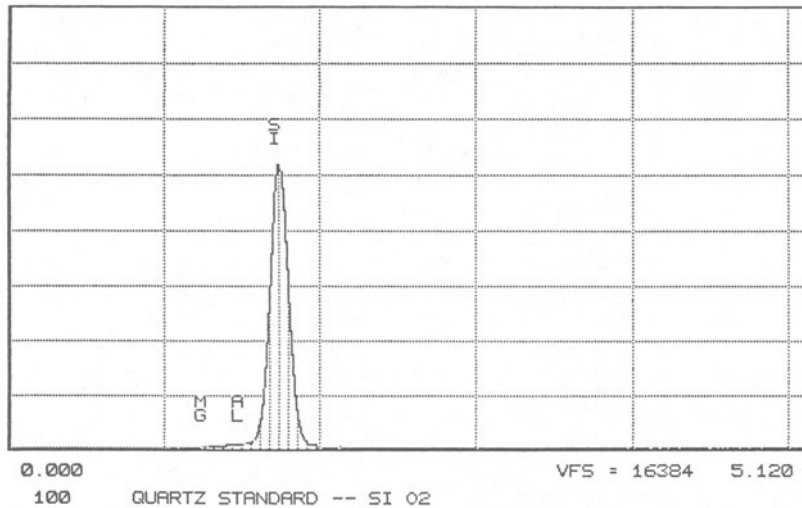


**Figure A19.8.** Silicon reference peak from  $\text{SiO}_2$  standard.

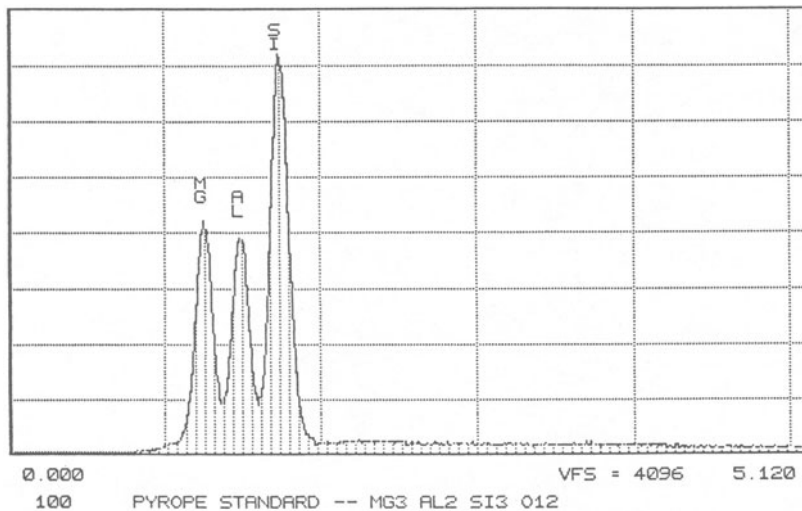


**Figure A19.9.** Mg-Al-Si reference spectrum from the mineral pyrope  $\text{Mg}_3\text{Al}_2\text{Si}_3\text{O}_{12}$ .

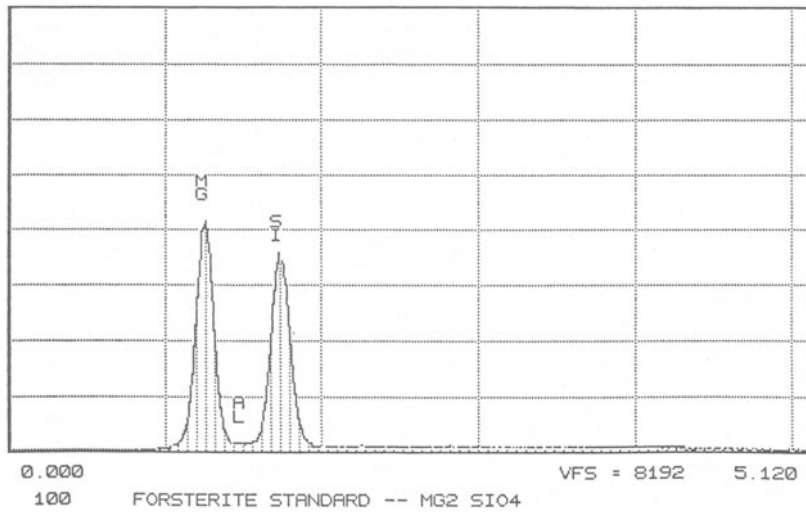


**Figure A19.10.** Mg-Si reference spectrum from the mineral forsterite  $Mg_2SiO_4$ .

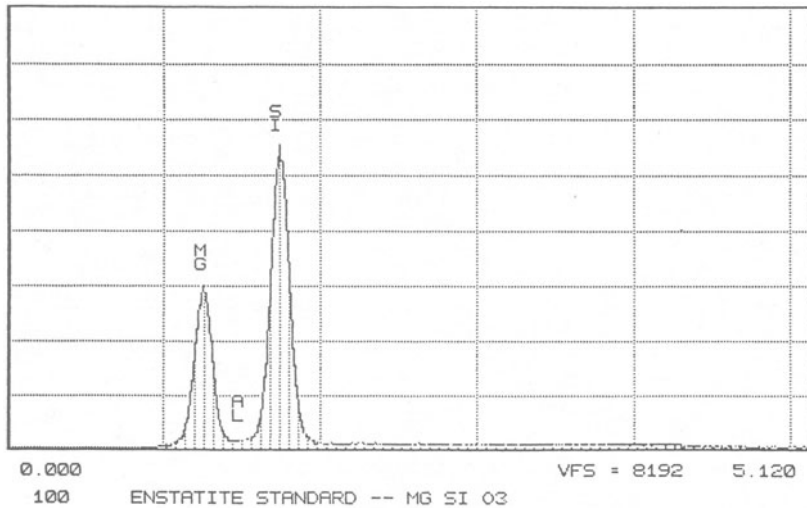


**Figure A19.11.** Mg-Si reference spectrum from the mineral enstatite  $MgSiO_3$ .

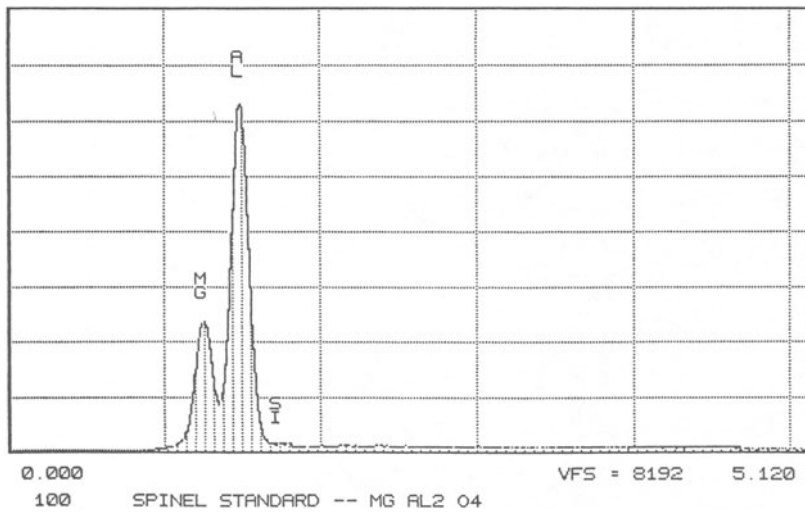


**Figure A19.12.** Mg-Al reference spectrum from the mineral spinel  $\text{MgAl}_2\text{O}_4$ .

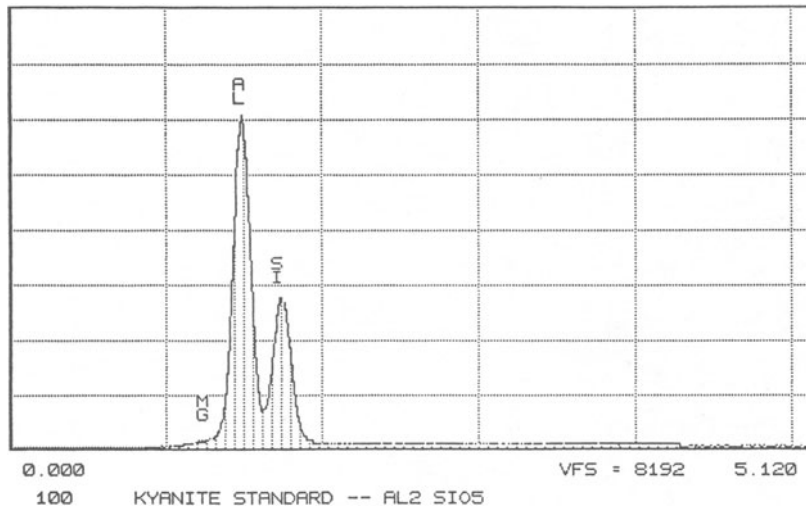


**Figure A19.13.** Al-Si reference spectrum from the mineral kyanite  $\text{Al}_2\text{SiO}_5$ .

**Table A19.8** Silicate Analyses using EDS at 15 kV

Sample	Actual oxide wt%	EDS analysis results		
		Standards	Semistd	No stds
<b>Mg<sub>2</sub>SiO<sub>4</sub></b>	MgO	57.30	57.50	57.56
	Al <sub>2</sub> O <sub>3</sub>	0.01	0.00	0.66
	SiO <sub>2</sub>	47.70	42.47	51.63
	CaO	0.05	0.06	0.10
	FeO	0.01	0.17	0.00
	Total	100.00	100.04	99.96
<b>MgSiO<sub>3</sub></b>	MgO	40.15	40.12	30.44
	Al <sub>2</sub> O <sub>3</sub>	0.01	0.00	0.74
	SiO <sub>2</sub>	59.85	59.80	68.71
	CaO	0.01	0.09	0.07
	FeO	0.01	0.09	0.00
	Total	100.00	100.04	99.96
<b>MgAl<sub>2</sub>O<sub>4</sub></b>	MgO	28.33	28.17	22.97
	Al <sub>2</sub> O <sub>3</sub>	71.67	71.70	76.51
	SiO <sub>2</sub>	0.10	0.00	0.38
	CaO	0.01	0.03	0.03
	FeO	0.05	0.10	0.08
	Total	100.00	100.03	99.98
<b>Al<sub>2</sub>SiO<sub>5</sub></b>	MgO	0.33	0.00	0.56
	Al <sub>2</sub> O <sub>3</sub>	62.92	63.16	62.70
	SiO <sub>2</sub>	37.08	36.43	36.43
	CaO	0.01	0.03	0.07
	FeO	0.01	0.21	0.09
	Total	100.00	99.95	99.86
<b>Mg<sub>3</sub>Al<sub>2</sub>Si<sub>3</sub>O<sub>12</sub></b>	MgO	30.00	30.08	22.90
	Al <sub>2</sub> O <sub>3</sub>	25.29	25.00	25.92
	SiO <sub>2</sub>	44.71	45.02	51.08
	CaO	0.06	0.09	0.05
	FeO	0.03	0.15	0.01
	Total	100.00	100.20	99.95

## Laboratory 20

# Light Element Microanalysis

### 20.1 Data Collection for Light Element Analysis

---

#### **Experiment 20.1: Carbon K Peak Shape.**

##### **Pure Carbon**

(a) Operating conditions: accelerating voltage = 10 kV, take-off angle = 40.0°, beam current = 110 nA. For carbon, a lead stearate crystal was used. All specimens were aluminum coated at the same time to minimize x-ray absorption.

(b) A WDS scan for graphite is shown in Figure A20.1. The scan is from 0.229 keV to 0.346 keV. The  $CK_{\alpha}$  peak is at 0.276 keV.

(c) Integrated peak intensity is 81,741 counts in 5 sec.  $\sqrt{N}/Nx100 = 0.35\%$ .

(d) Average background intensity is 716 counts in 5 sec.

(e) No EDS measurements were made.

##### **Iron Carbide, $Fe_3C$**

(a) A WDS scan for  $Fe_3C$  is shown in Figure A20.2. The scan is again from 0.229 keV to 0.346 keV.

(b) The  $CK_{\alpha}$  peak is at 0.275 keV. Two other strong peaks are shown,  $FeL1$  second order ( $n=2$ ) at about 0.315 keV and  $FeL_{\alpha}$  third order at 0.235 keV. The presence of these iron L peaks makes measurement of carbon background difficult. The graphite scan (Figure A20.1) does not include the  $FeL$  peaks. In addition, the carbon peak in  $Fe_3C$  is at a slightly lower energy (~1 eV lower).

(c) Peak intensity is 46,643 counts in 58 sec  $\sqrt{N}/Nx100 = 0.46\%$ . Average background intensity is 3,882 in 58 sec.

(d) No EDS measurements were made.

#### Questions

1. For the light elements the electrons that fill the vacancy in the K-shell often come from the valence band; thus, the K-spectra often show evidence of chemical bonding of the element wavelength shifts and peak shape changes.
  2. The  $Fe_3C$  standard provides a reproducible standard much more like steel since carbon atoms are surrounded by iron atoms as in the steel. Accurate quantitative analysis of light elements requires the use of integrated intensities if the peak shape varies with chemical bonding. Maximum peak height measurements can only be used if there is no difference in peak shape between sample and standard.
  3. The energy resolution of the EDS detector is not sufficient to detect chemical shifts or changes in peak shape.
- 

---

#### **Experiment 20.2: Background Intensity.**

**Method 1:** The carbon  $K_{\alpha}$  intensity in  $Fe_3C$  is 45,740 counts in 61 sec. The carbon off-peak background intensity on the  $Fe_3C$  is 2,777 counts in 61 sec.

**Method 2:** The "carbon background" measured on pure iron at the carbon peak position is 4,380 counts in 61 sec.

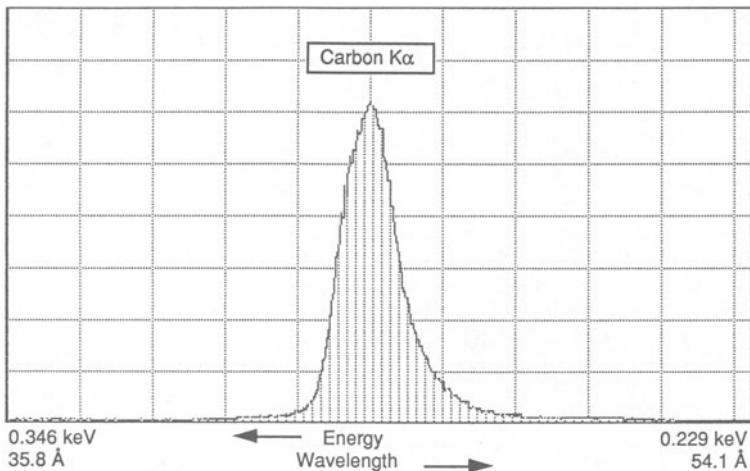


**Figure A20.1.** WDS 2θ-scan across the carbon  $K_{\alpha}$  peak on graphite. Peak maximum is at 276 eV (44.8 Å). Counting time = 5 sec.  $E_0 = 10$  keV. Maximum intensity, vertical full scale (VFS) = 2048.

### Questions

1. The carbon background on pure iron at the carbon peak position (Method 2) is clearly higher than that measured from the  $Fe_3C$  off-peak intensities. If off-peak positions for background are measured on pure iron, the carbon background is 2,716 counts in 61 sec. This background value compares favorably with that obtained from  $Fe_3C$  (Method 1). The apparent carbon intensity measured at the carbon peak position on pure iron is real. Apparently a layer of carbon was deposited on the surface of the pure iron during either sample preparation, sample coating, the transfer process into the instrument, evacuation of the instrument, or analysis.

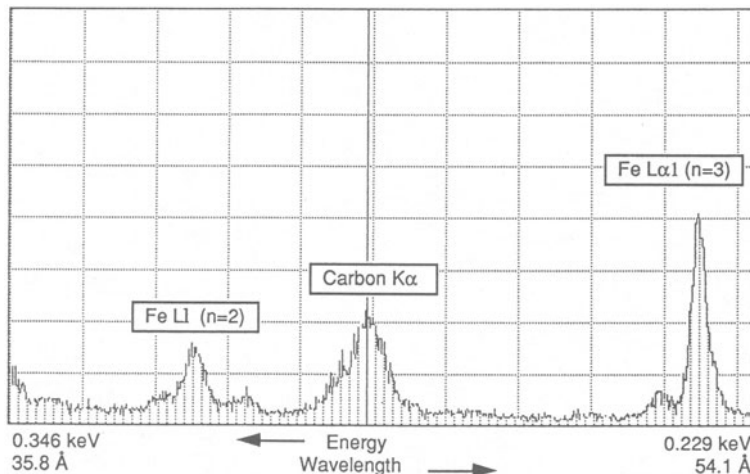


**Figure A20.2.** WDS 2θ-scan across the carbon  $K_{\alpha}$  peak on  $Fe_3C$ . Peak maximum is at 275 eV (45.0 Å). Counting time 58 sec.  $E_0 = 10$  keV. FeL peaks are also visible. Maximum intensity, vertical full scale (VFS) = 256.

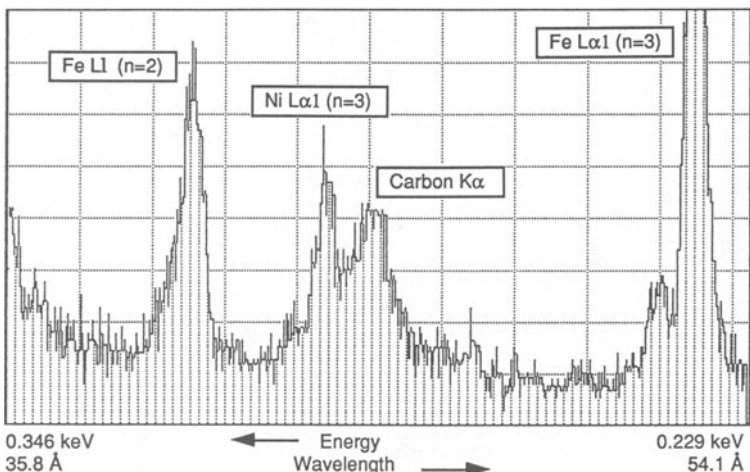


**Figure A20.3.** WDS 2θ-scan across carbon peak with pulse height analyzer open. Maximum intensity, vertical full scale (VFS) = 64.

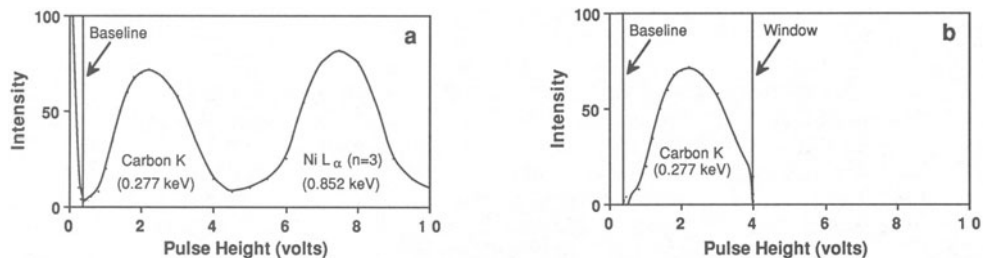


**Figure A20.4.** Schematic pulse height distribution curves. (a) PHD curve for Figure A20.3 showing acceptance of overlapping carbon and nickel signals. (b) PHD curve for Figure A20.5 showing rejection of iron and nickel signals by restricting the energy of the pulses that are accepted.

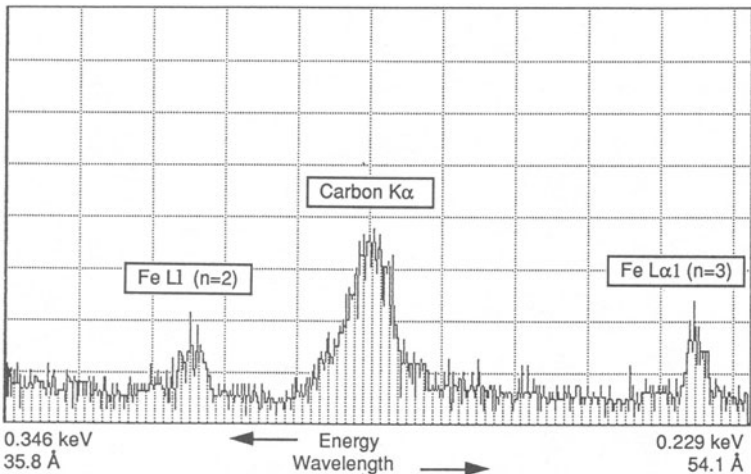


**Figure A20.5.** WDS 2θ-scan across carbon  $K_{\alpha}$  peak with PHA adjusted to allow only the carbon peak to be accepted. Maximum intensity, vertical full scale (VFS) = 64.

- The most accurate method for determining continuum background is to measure the off-peak background directly on the sample.
  - WDS has several advantages over EDS for background measurements of the light elements. Among these are the ability to avoid overlapping  $L$  and  $M$  peaks, to avoid the high EDS background at low energies, and to utilize high count rates for better detectability and precision ( $\sqrt{N}/N$  effects).
- 

#### **Experiment 20.3: Peak Overlaps.**

(a) A wavelength scan was run through the carbon peak using a Fe-9.9 wt% Ni-1.04 wt% C standard, as shown in Figure A20.3. A detector voltage of 1850 V was used and the pulse height analyzer (PHA) was set at 0.4 V base line and 10 V window (wide open). The carbon peak position is indicated at 0.277 voltage. The  $FeL$  peaks, as observed in the  $Fe_3C$  scan of Figure A20.2, are also present in this WDS scan. The  $NiL_\alpha$  has an energy of 0.8502 voltage and a wavelength of 14.56 Å. The third order  $NiL_\alpha$  line appears at a  $n\lambda$  value of 43.68 Å or an equivalent energy of 0.284 voltage, very close (within 7 ev) to the  $CK_\alpha$  peak in the Fe-Ni-C standard. Figure A20.4a shows a schematic pulse height distribution curve for the carbon peak position of Figure A20.3. The third order  $NiL_\alpha$  may diffract at the same angle as  $CK_\alpha$  but the x-rays are of higher energy and thus give rise to a separate pulse height.

(b) The pulse height analyzer was adjusted to exclude most of the high energy (0.852 voltage) x-ray peak from  $NiL_\alpha$  as shown in Figure A20.4b. The new PHA settings were 0.4 V base line, a 4.0-V window. Figure A20.5 shows a wavelength scan over the same range as Figure A20.3. The interfering  $NiL_\alpha$  third-order peak is not present and the  $FeL$  higher-order peaks are much smaller.

---

## **20.2 Measurement of Light Element Concentrations**

**Experiment 20.4: Quantitation by the ZAF Method.** The measurements from the  $Fe_3C$  standard are

$$CK_\alpha \text{ peak intensity } I_{\text{carbon}}^{\text{std}} \text{ on } Fe_3C = 49,628 \text{ counts in 56 sec}$$

$$CK_\alpha \text{ background intensity } I_{\text{carbon}}^{\text{std bg}} \text{ on } Fe_3C = 3,828 \text{ counts in 56 sec}$$

$$I_{\text{std}} = I_{\text{carbon}}^{\text{std}} - I_{\text{carbon}}^{\text{std bg}} = 49,628 - 3,828 = 45,800 \text{ counts}$$

The measurements from the homogeneous steel sample are

$$CK_\alpha \text{ peak intensity } I_{\text{carbon}} \text{ from the steel sample} = 11,090 \text{ counts in 56 sec}$$

$$\text{sec} \quad CK_\alpha \text{ background } I_{\text{carbon}}^{\text{bg}} \text{ measured directly on the steel sample} = 3,174 \text{ counts in 56 sec}$$

$$I_{\text{SAMPLE}} = I_{\text{carbon}} - I_{\text{carbon}}^{\text{bg}} = 11,090 - 3,174 = 7,916$$

The ratio of carbon x-ray intensity from the steel sample to that from the  $Fe_3C$  carbon standard,  $K_{\text{carbon}}$ , is given by

$$K_{\text{carbon}} = I_{\text{SAMPLE}}/I_{\text{STD}} = 7,916/45,800 = 0.173$$

If the correction factors in ZAF are equal 1.0 and the carbon content of  $Fe_3C$  is 6.67 wt%, then the uncorrected carbon content of the homogeneous steel sample is 1.15 wt%. With correction for carbon absorption in the steel, and using the measured data for iron (standard and background intensities), the ZAF program gives the measured carbon content in the steel as 0.8 wt%.

---

**Table A20.1.** Calibration Curve Data

Alloy	C Peak	C Backgnd	Peak-backgnd
Fe	8,544	5,747	2,797
0.30 C	12,785	5,617	7,168
0.62 C	16,205	5,766	10,439
1.01 C	22,366	5,865	16,501
1.29 C	27,863	5,811	22,052
Steel	19,430	5,661	13,796
unknown			

**Experiment 20.5: Quantitation by the Calibration Curve Method.** To obtain the calibration curve, four Fe-C standards were used plus pure iron. The standards contained 0.30, 0.62, 1.01, and 1.29 wt% C. Data were taken at 10 kV, 147 nA, 100 sec counting time, and 40.0° take-off angle. The average data for each alloy are given in Table A20.1. The carbon x-ray intensity (peak-backgnd) versus carbon concentration curve is plotted in Figure A20.6. The carbon intensity does not go to zero when the carbon content is zero for the reasons discussed in Question 1, Experiment 20.2. The calibration curve is almost linear as shown by the best straight line drawn through the data. The value of  $I_{\text{Peak-Background}}$  for the steel unknown is 13,769 as shown in the data above. Using the calibration curve (Figure A20.6) the value of the carbon concentration in the steel sample is 0.81 wt%. This value compares favorably with the known carbon content of 0.80 wt%.

#### Questions

1. The two methods of quantitation yielded very similar values of carbon content in the steel sample. The calibration method is more accurate since no calculations of absorption or atomic number effects are necessary.
2. If the operating voltage were increased, the absorption correction would become larger. However, as in Question 1, the calibration curve method would still be more accurate.

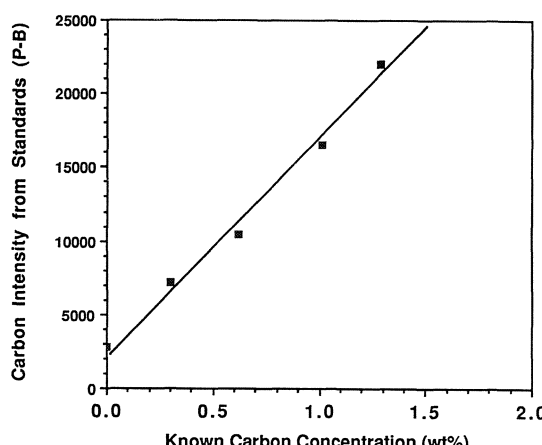


**Figure A20.6.** Carbon x-ray intensity (peak minus background) versus carbon concentration for the carbon in iron standards.

## Laboratory 21

# Trace Element Microanalysis

### 21.1 Data Collection for Trace Element Analysis

**Experiment 21.1: Data from a High-Phosphorus Standard.**

(a) WDS analysis of a meteoritic schreibersite standard ( $\text{FeNi}_3\text{P}$  with 15.5 wt% phosphorus. Accelerating voltage = 15 kV, take-off angle =  $40.0^\circ$ , beam current = 145 nA. For iron and nickel, a LiF crystal was used. For phosphorus, a PET crystal was used. The data are shown in Table A21.1.

**Table A21.1.** WDS Data from High-Phosphorus Standard

Element	Peak position (keV)	Background positions (keV)	$N_S$ (counts)	$N_{SB}$ (counts)	Time (sec)
$\text{Fe}K_\alpha$	6.406	6.222	6.603	384,711	970
$\text{Ni}K_\alpha$	7.484	7.233	7.753	61,000	1,311
$\text{P}K_\alpha$	2.013	1.973	2.054	400,061	1,297

(b) EDS. Accelerating voltage = 15 kV, take-off angle =  $40.0^\circ$ , beam current = 145 nA. The EDS collimator entrance size was made smaller using an adjustable aperture until the dead time was <20%. Counting time = 100 sec.

Figure A21.1 illustrates the EDS spectrum from the phosphide standard, 15.5 wt% P and Figure A21.2 shows the phosphorus peak and continuum background in more detail. Note the energy regions containing the full-width-at-half-maximum (FWHM). The iron and nickel peaks and backgrounds were also measured this way. The data are summarized in Table A21.2.

**Table A21.2.** EDS Data from High-Phosphorus Standard

Element	Peak position (keV)	FWHM (ev)	Background region (keV)		$N_{SB}$ (counts)		
			-	+	$N_S$ (counts)	-	+
$\text{Fe}K_\alpha$	6.40	140	6.02-6.16	6.66-6.80	28,814	864	704
$\text{Ni}K_\alpha$	7.48	180	6.66-6.80	7.82-8.00	3,581	704	520
$\text{P}K_\alpha$	2.02	120	1.74-1.86	2.24-2.36	16,740	2,706	1,641
							2,174

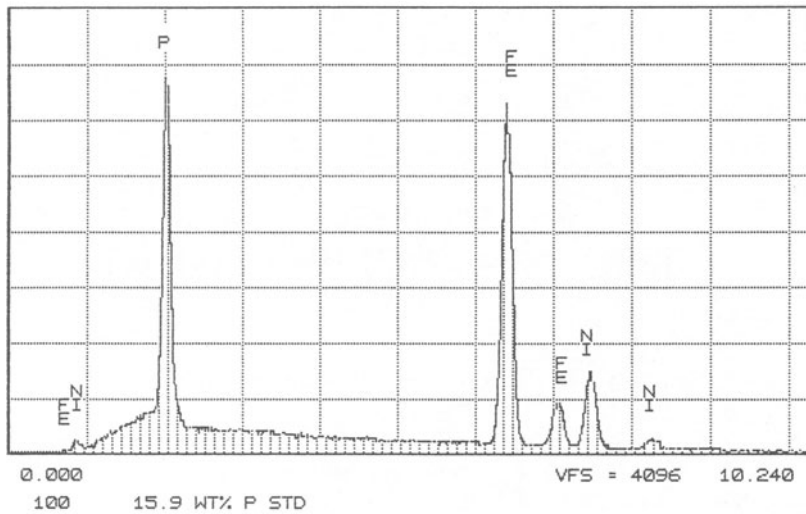


**Figure A21.1.** EDS spectrum from the phosphide standard (15.5 wt% P). X-ray energy range is 0 to 10.24 keV.

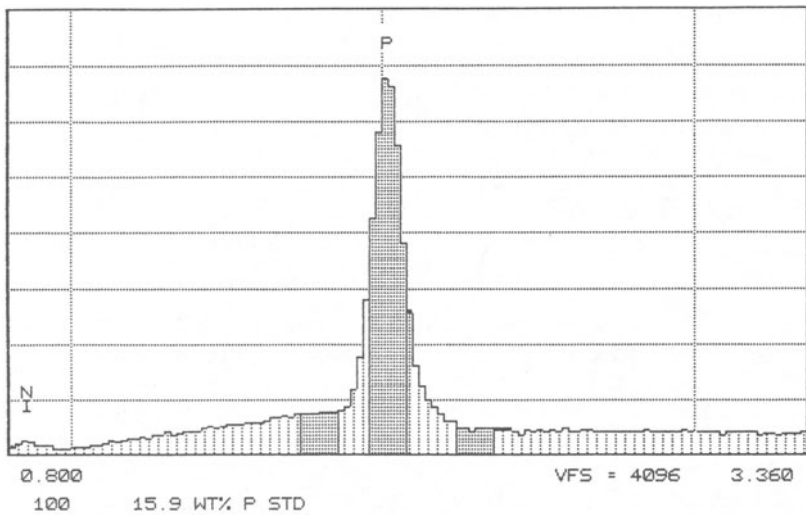


**Figure A21.2.** EDS spectrum around the phosphorus peak in Figure A20.1. Background windows are shown above and below peak.

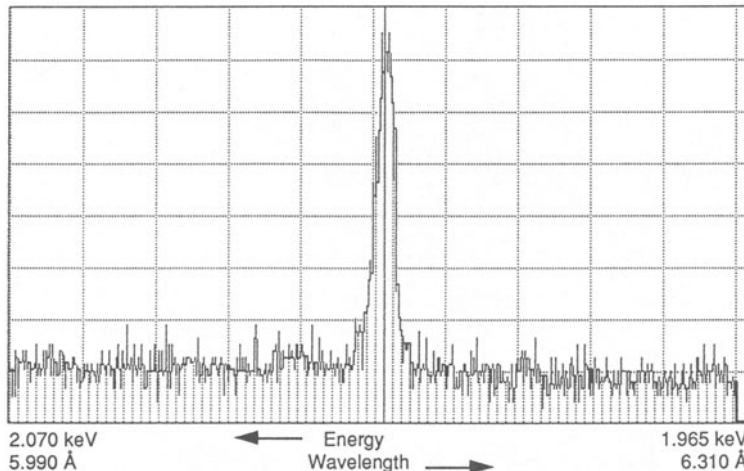


**Figure A21.3.** WDS 2 $\theta$  scan around the phosphorus peak position in the Fe-Ni-P alloy containing 0.35 wt%P. X-ray energy range is 1.965 to 2.070 keV. Minimum intensity vertical scale. Vertical fall scale = 64.

### **Experiment 21.2: Establishing the Background at Low Phosphorus Concentration.**

(a) Figure A21.3 shows the WDS scan around the phosphorus peak position on the Fe-Ni-P alloy containing 0.35 wt% P. The scan was taken over a 100-eV range from 1.965 to 2.070 keV. The continuum background positions are chosen  $\pm 30$  eV around the phosphorus peak at 2.043 keV and 1.983 keV. The data for  $N_B$  determination are shown in Table A21.3.

(b) Figures A21.4 and A21.5 show EDS spectra on the 0.35 wt% Fe-Ni-P alloy taken for 100 sec and 400 sec, respectively. The  $PK_{\alpha}$  peak at 2.103 keV is hardly visible. Figure A21.6 shows an expanded region around the phosphorus peak. Note that the peak is visible above background after 400 sec but is indistinguishable from background after only 100 sec. The data for  $N_B$  are shown in Table A21.4.

**Table A21.3.** WDS Data from Low-Phosphorus Standard (WDS, Counting Time = 100 sec)

Element	Background Positions (keV) and Intensity (counts)				$N$ (counts)	$N_B$ (counts)
	-(keV)	(counts)	+(keV)	(counts)		
Phosphorus	1.983	1,022	2.043	1,912	11,469	1,467

**Table A21.4.** EDS Data from Low-Phosphorus Standard (EDS, Counting Time = 100 sec)

Element	FWHM (keV)	Background regions (keV)		$N$ (counts)	$N_B$ (counts)		
		-	+		-	+	Ave.
Phosphorus	120	1.74-1.86	2.24-2.36	1,810	1,889	1,769	1,829

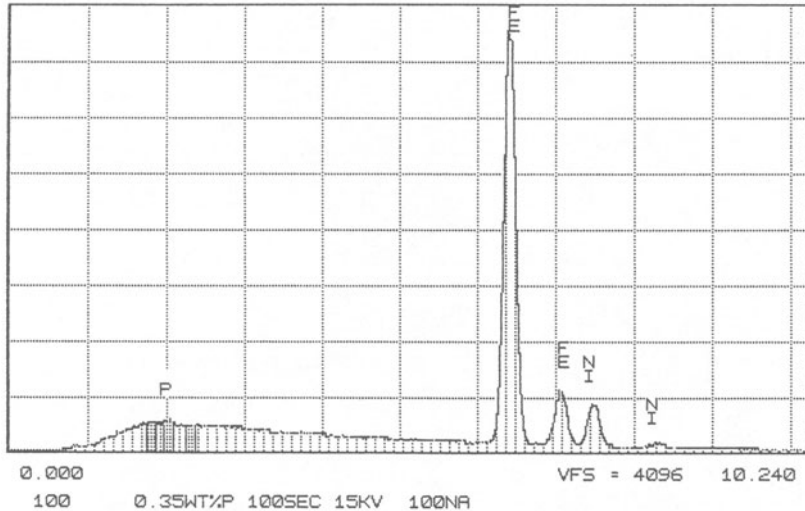


**Figure A21.4.** EDS spectrum from the Fe-Ni-0.35P alloy taken with a counting time of 100 sec. X-ray energy range is 0 to 10.24 keV. The position of the phosphorus  $K_{\alpha}$  line is 2.014 keV.

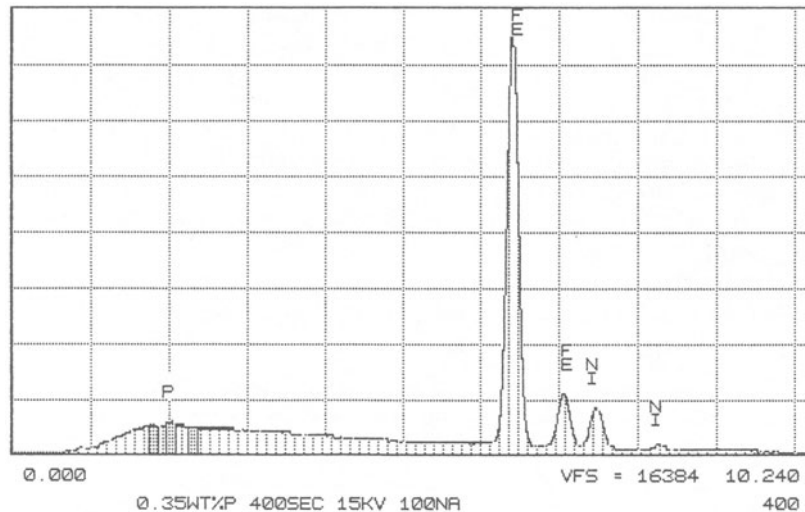


**Figure A21.5.** EDS spectrum from the Fe-Ni-0.35P alloy taken with a counting time of 400 sec.

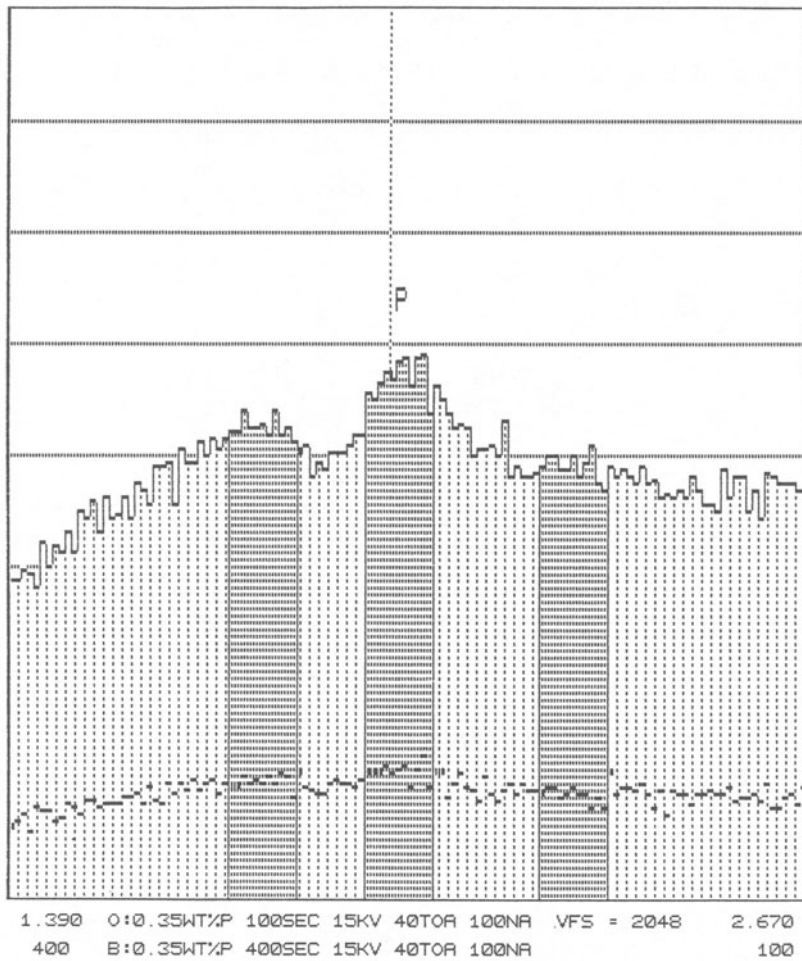


**Figure A21.6.** Expanded EDS region from the Fe-Ni-0.35P alloy spectra of Figures A21.4 and A21.5 collected with 400 sec counting time (top) and 100 sec counting time (bottom). X-ray energy range is 1.390-2.670 keV.

Note in Figure A21.6 that the 100-sec data  $N$  is essentially the same as  $N_B$ . Even for a 400-sec counting time,  $N = 7,308$  and  $N_B = 7,348$ . Thus, using a set of regions above and below the phosphorus peak, we are not able to distinguish the presence of phosphorus although the phosphorus peak is apparently present. A background fitting technique may be more useful in determining  $N_B$ , since the background around the phosphorus peak is not symmetrical (see Figures A21.1 and A21.2).

## 21.2 Minimum Detectability Limits

---

**Experiment 21.3: Estimation of Minimum Detectability from Alloy Data.** To estimate a minimum detectability limit,  $C_{DL}$ , we assume  $N - N_B$  in equation (21.1) just equals  $3(N_B)^{1/2}$ . Thus,

$N_B$ (WDS) on 0.35 wt% P alloy = 1,467 counts,  $3(N_B)^{1/2} = 114.9$

$N_B$ (EDS) on 0.35 wt% P alloy = 1,829 counts,  $3(N_B)^{1/2} = 128.3$

$N_S$ (WDS) on 15.5 wt% phosphide = 400,061 counts,  $N_{SB} = 1,297$

$N_S$ (EDS) on 15.5 wt% phosphide = 16,740 counts,  $N_{SB} = 2,174$

$$C_S = 15.5 \text{ wt\%}$$

Using equation (21.1),

$$C_{DL} = \left( \frac{N - N_B}{N_S - N_{SB}} \right) C_S = \left[ \frac{3(N_B)^{1/2}}{N_S - N_{SB}} \right] C_S \quad (21.1)$$

For WDS,

$$C_{DL} = 0.0045 \text{ wt\%, } 45 \text{ ppm}$$

For EDS,

$$C_{DL} = 0.135 \text{ wt\%, } 1350 \text{ ppm}$$

#### ***Experiment 21.4: Estimation of Minimum Detectability from Pure Element Standards.***

For the Ziebold equation,

$$C_{DL} = (3.29A)/(tP^2/B)^{1/2} \quad (21.2)$$

we use the following data to calculate  $C_{DL}$ .

Factor	WDS	EDS
$A$	1.0	1.0
$t$	100 sec	100 sec
$P = N - N_B$	24,000 cps	1,000 cps
$B = N_B$	78 cps	130 cps
$C_{DL}$ (wt%)	0.012 wt%	0.375 wt%

The  $C_{DL}$  values determined by the Ziebold equation are more conservative, that is, about three times higher than those measured in Experiment 21.3.

#### Questions

1. The  $C_{DL}$  values are 30 times larger using EDS rather than WDS. Clearly the WDS technique yields a much improved detectability limit, well below 100 ppm. The WDS technique is better because the  $P$  and  $P/B$  values are so much higher for the same counting time.
2. The meteorite contains a  $P$  concentration 0.08wt%. The detectability limit for  $P$  using EDS is 0.135wt%. Therefore the EDS cannot detect the presence of  $P$  in the meteorite.

**Table A21.5.** Phosphorus Measurement Using WDS in a Meteorite

Point No.	Ni(counts)		Fe(counts)		P(counts)	
	N	N <sub>B</sub>	N	N <sub>B</sub>	N	N <sub>B</sub>
1	196,717	12,700	4,177,151	9094	2163	1014
2	205,735	12,563	4,210,170	9032	2210	1143
3	201,352	12,737	4,197,295	9061	2176	1100
4	201,760	12,444	4,208,298	9174	2143	1114
5	204,221	12,833	4,191,416	9071	2036	1100
6	204,477	12,743	4,167,921	9329	2159	1099

## 21.3 Measurement of Trace Element Concentrations

### *Experiment 21.5: Measurement of P Content in a Meteorite.*

(a) Since  $C_{DL}$  for P was too high to measure using EDS, only WDS measurements were made in the low-nickel kamacite phase of the meteorite. The data from several positions in the meteorite are shown in Table A21.5. The analysis conditions for WDS were 15 kV, 145 nA beam current, and 100 sec counting time. The WDS scan around the phosphorus peak on the kamacite phase in the iron meteorite at 2.103 kV is shown in Figure A21.7. The scan ranges from 1.965 kV to 2.070 kV. The  $PK_{\alpha}$  peak can be clearly seen above the background.

(b) The ZAF technique was chosen for the analysis of the metal phase. For point 1 in Table A21.5, the phosphorus concentration in the meteorite was 0.08 wt%. The ZAF factors shown in Table A21.6 were used to compute the wt% for each element from the K ratios:

$$K \text{ ratio} = \frac{N - N_B}{N_S - N_{SB}}$$

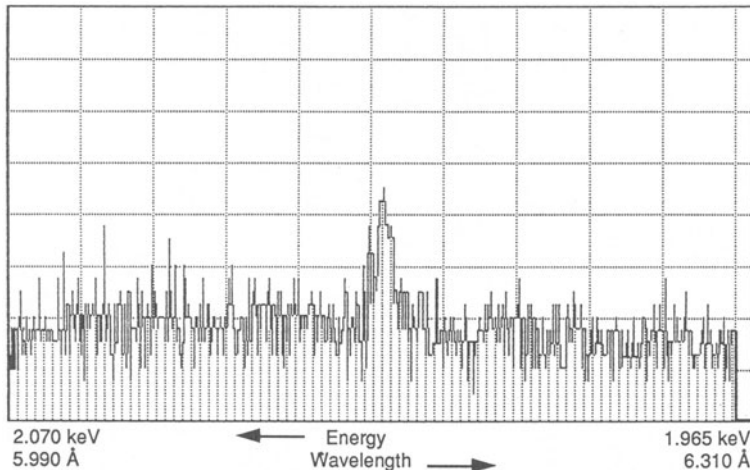


**Figure A21.7.** WDS 2θ scan around the phosphorus peak on the meteorite kamacite phase (low-nickel bcc phase) containing approximately 0.08wt%P. The scan covers an energy range of 1.965-2.070 keV. Maximum intensity vertical scale. Vertical fall scale = 32.

**Table A21.6** Chemical Analysis Using ZAF Technique

Element	K ratio	Z	A	F	ZAF	wt%
Fe	0.946	1.001	1.0	0.995	0.996	94.3
Ni	0.044	0.985	1.06	1.0	1.044	4.6
P	0.0006	0.927	1.418	0.998	1.313	0.08

(c) Calculation of  $C_{DL}$  for Point 1, Table A21.5:

$$C_{DL} = \left( \frac{N - N_B}{N_S - N_{SB}} \right) C_S$$

where  $N - N_B = 3(N_B)^{1/2}$  (Equation 21.1). From Table A21.5, Point 1,  $N_B = 1014$  counts,  $3(N_B)^{1/2} = 95.5$ . From Table A21.1,  $N_S = 400,061$  counts,  $N_{SB} = 1,297$  counts, and  $C_S = 15.5\text{ wt\%}$ . Therefore,

$$C_{DL} = \frac{95.5}{(400,061 - 1,297)} (15.5)\text{wt\%} = 0.0037 \text{ wt\% (37 ppm)}$$

Thus,  $C_{DL}$  is well below the phosphorus content in kamacite of 0.08 wt%.

(d) Phosphorus content in kamacite =  $0.08 \pm 0.0037$  wt%.

## Laboratory 22

# Particle and Rough Surface Microanalysis

## 22.2 Spherical Particles or Fracture Surfaces

---

**Experiment 22.1: The Microscope-Detector Relationship.** (a) While many modern SEMs have EDS detectors mounted such they they look down on the specimen with a known take-off angle (at one particular working distance), most SEMs have EDS detectors that have an arbitrary relationship to the specimen. If the specimen lies below the detector and is tilted toward the detector, the take-off angle  $\psi$  may be calculated from

$$\psi = \theta + \arctan(\Delta z/x)$$

where  $\theta$  is the specimen tilt angle,  $\Delta z$  is the distance that the beam impact point on the specimen is below the detector chip center line, and  $x$  is the distance between the detector chip and the electron beam impact point on the specimen. More details of this measurement may be found in *SEM XM*, p. 337.

(b) The relative position of the detector on the image may be found by viewing the specimen chamber from the top in the same orientation as the micrograph and noting the detector orientation.

(c) As shown in (a) the specimen should be kept at the same height, tilt angle, and  $x$ - $y$  translation for each quantitative microanalysis.

---

**Experiment 22.2: Rastered Beam and Point Analyses (Method 1).** One can observe in Table A22.1 that conventional EDS methods produce very poor results. Results for the point analyses are particularly bad. The measured  $\text{Al}K_{\alpha}$  peak intensity for the point analysis on the particle on the side away from the detector is only 6% of that measured on the flat specimen, while the  $\text{Ni}K_{\alpha}$  intensity measured on the same point is over 85% of that measured on the flat specimen. If the flat specimen were used as a standard as in Method 1 (Section 22.1), the ZAF processed EDS composition results would be as shown in Table A22.2. The relative errors for the normalized results with both the rastered beam and the point analysis toward the detector are about 10%, whereas the relative error in aluminum for the point analysis away from the detector is more than 85%. The  $\text{Al}K_{\alpha}$  intensity is down, compared to the  $\text{Ni}K_{\alpha}$ , because of that x-ray line's much greater absorption by the sample and the longer path length, relative to the flat specimen, that x-rays must travel to leave the specimen.

---

**Experiment 22.3: Peak-to-Background Ratios (Method 2).** The peak-to-background ratios for  $\text{Al}K_{\alpha}$  and  $\text{Ni}K_{\alpha}$  in the point analyses of the NiAl particle, as shown in Table A22.2, are certainly more constant than the peak intensities; however, there is still significant variation. The peak-to-background ratios for  $\text{Al}K_{\alpha}$  for the point analyses (12.2 and 9.08) as given in Table A22.2 differ by as much as 20% relative to the value for the flat

**Table A22.1.** Example Data from Experiments 22.2-22.4Take-off angle: 40°

		Flat specimen	Whole ptc specimen	Side of particle	
20 keV				Toward detector	Away from detector
Intensity:	$\text{Ni}L_\alpha$	16,029	9,207	21,543	1,568
	$\text{Al}K_\alpha$	127,526	86,647	180,359	8,317
	$\text{Ni}K_\alpha$	153,208	89,783	155,316	132,202
Background:	$\text{Ni}L_\alpha$	3,237	2,895	4,720	258
	$\text{Al}K_\alpha$	12,621	13,371	14,820	916
	$\text{Ni}K_\alpha$	9,114	9,180	9,142	8,485
Relative intensity:	$\text{Al}K_\alpha/\text{Ni}K_\alpha$	0.834	0.965	1.16	0.063
	$\text{Al}K_\alpha/\text{Ni}L_\alpha$	7.960	9.410	7.21	5.300
Peak/back-ground:	$P/B \text{ Ni}L_\alpha$	4.95	3.18	4.56	6.09
	$P/B \text{ Al}K_\alpha$	10.10	6.48	12.20	9.08
	$P/B \text{ Ni}K_\alpha$	16.80	9.78	17.00	15.60
<b>10 keV</b>					
Intensity:	$\text{Ni}L_\alpha$	13,881	4,829	16,179	3,429
	$\text{Al}K_\alpha$	85,263	39,027	99,372	16,151
	$\text{Ni}K_\alpha$	4,015	1,508	4,022	3,922
Background:	$\text{Ni}L_\alpha$	3,248	1,604	3,994	562
	$\text{Al}K_\alpha$	11,287	6,717	12,864	2,259
	$\text{Ni}K_\alpha$	1,819	1,257	1,655	1,659
Relative intensity:	$\text{Al}K_\alpha/\text{Ni}K_\alpha$	21.20	25.90	24.70	4.12
	$\text{Al}K_\alpha/\text{Ni}L_\alpha$	6.14	8.08	6.14	4.71
Peak/back-ground:	$P/B \text{ Ni}L_\alpha$	4.27	3.01	4.05	6.10
	$P/B \text{ Al}K_\alpha$	7.55	5.81	7.72	7.15
	$P/B \text{ Ni}K_\alpha$	2.20	1.20	2.43	2.36

specimen (10.1). The peak-to-background values for the less-absorbed  $\text{Ni}K_\alpha$  are closer to that less-absorbed  $\text{Ni}K_\alpha$  are closer to that for the flat specimen (17.0 and 15.6 versus 16.8), differing by less than 7.5% relative to the flat sample. On the other hand, the peak-to-background ratios for the whole particle scan are 35% to 45% lower than the peak-to-background ratio for the flat specimen. This is because rastering the beam over the whole particle surface results in some of the beam electrons penetrating into the substrate on which the particle sits. As a result, the background continuum contains contributions from both particle and substrate while the characteristic x-ray peaks come only from the particle since the substrate does not contain nickel or aluminum. If the example data were processed using Equation 22.1 and the ZAF method, the results would look like those of Table A22.3.

**Table A22.2.** 20 kV EDS/ZAF Compositions of NiAl Particles from Peak Intensities (Method 1)

Unnormalized	Actual (wt%)	Rastered beam	Point analyses	
			Toward detector	Away from detector
Al	31.49	22.94	40.58	2.67
Ni	68.51	41.14	69.42	59.50
TOTAL	100.00	64.08	110.00	62.17
<b>Normalized</b>				
Al	31.49	35.80	36.89	4.29
Ni	68.51	64.20	63.11	95.71
TOTAL	100.00	100.00	100.00	100.00
<b>Atom fractions</b>				
Al	0.500	0.548	0.560	0.089
Ni	0.500	0.452	0.440	0.911

**Table A22.3.** 20 kV EDS/ZAF Compositions of NiAl Particles from Peak-to-Background Ratios (Method 2)

Unnormalized	Actual (wt%)	Rastered beam	Point analyses	
			Toward detector	Away from detector
Al	31.49	20.20	38.04	28.31
Ni	68.51	39.88	69.33	63.62
TOTAL	100.00	60.09	107.36	91.93
<b>Normalized</b>				
Al	31.49	33.62	35.43	30.80
Ni	68.51	66.38	64.57	69.20
TOTAL	100.00	100.00	100.00	100.00
<b>Atom fractions</b>				
Al	0.500	0.524	0.544	0.492
Ni	0.500	0.476	0.456	0.508

**Table A22.4.** 10 kV EDS/ZAF Compositions of NiAl Particles from Peak Intensities (Method 1)

Unnormalized	Actual (wt%)	Rastered beam	Point analyses	
			Toward detector	Away from detector
Al	31.49	15.35	36.01	6.59
Ni	68.51	24.53	79.29	17.49
TOTAL	100.00	39.80	115.30	24.07
<b>Normalized</b>				
Al	31.49	38.49	31.23	27.36
Ni	68.51	61.51	68.77	72.64
TOTAL	100.00	100.00	100.00	100.00
<b>Atom fractions</b>				
Al	0.500	0.577	0.497	0.450
Ni	0.500	0.423	0.503	0.550

**Experiment 22.4: Low Voltage.** Table A22.1 shows that performing these analyses at 10 keV (using the  $\text{Al}K_{\alpha}$  and  $\text{Ni}L_{\alpha}$  lines) somewhat improves results using peak intensities relative to those at 20 keV, but somewhat degrades results using peak-to-background ratios. The results using peak intensities are improved because (1) there is less absorption of the low-energy x-ray lines at 10 keV than there is at 20 keV, thus lessening the effect of differences in x-ray path length between particle and flat specimen, and (2) the  $\text{Ni}L_{\alpha}$  is closer in energy and absorption properties to the  $\text{Al}K_{\alpha}$  line than is the  $\text{Ni}K_{\alpha}$  line. However, while the results using peak intensities are improved, they still are not good. Processing these intensity data to give compositions would result in analyses similar to those of Tables 22.4 and 22.5.

**Table A22.5.** 10 kV EDS/ZAF Compositions of NiAl Particles from Peak-to-Ratios (Method 2)

Unnormalized	Actual (wt%)	Rastered beam	Point analyses	
			Toward detector	Away from detector
Al	31.49	24.23	32.20	29.82
Ni	68.51	48.79	64.98	97.87
TOTAL	100.00	72.53	97.18	127.69
<b>Normalized</b>				
Al	31.49	33.41	33.13	23.35
Ni	68.51	66.59	66.87	76.65
TOTAL	100.00	100.00	100.00	100.00
<b>Atom fractions</b>				
Al	0.500	0.522	0.519	0.399
Ni	0.500	0.481	0.481	0.601

**Table A22.6. Experiment 22.5**

**Rastered beam analysis**  
Accelerating potential: 15 keV

Diameter: Shape:	<u>Thick</u> Flat	<u>12 <math>\mu\text{m}</math></u> Trig.pr.	<u>4 <math>\mu\text{m}</math></u> Tetr.pr.		
K-ratio:	$\text{Mg}K_{\alpha}$	1	0.1846	0.2792	—
	$\text{Si}K_{\alpha}$	1	0.1816	0.2450	—
	$\text{Ca}K_{\alpha}$	1	0.2104	0.2291	—
	$\text{Fe}K_{\alpha}$	1	0.2278	0.2524	—
R-factor:	Mg/Si	1	1.017	1.140	—
	Ca/Si	1	1.159	0.935	—
	Fe/Si	1	1.250	1.030	—

**From Figures A22.1-A22.3 (calculated):**

R-factor:	Mg/Si	1	1.03	1.10	—	—
	Ca/Si	1	1.16	0.92	—	—
	Fe/Si	1	1.27	1.01	—	—

**Point beam analyses**

Accelerating potential: 15 keV

Diameter: Shape:	<u>Thick</u> Flat	<u>4 <math>\mu\text{m}</math></u> Trig.pr	<u>2 <math>\mu\text{m}</math></u> Tetr.pr		
K-ratio:	$\text{Mg}K_{\alpha}$	1	0.9518	0.3400	—
	$\text{Si}K_{\alpha}$	1	1.2260	0.2640	—
	$\text{Ca}K_{\alpha}$	1	0.7298	0.2504	—
	$\text{Fe}K_{\alpha}$	1	0.7080	0.2880	—
R-factor:	Mg/Si	1	0.7763	1.288	—
	Ca/Si	1	0.5953	0.948	—
	Fe/Si	1	0.5775	1.091	—
P/B:	$\text{Mg}K_{\alpha}$	360.4	270.7	115.4	—
	$\text{Si}K_{\alpha}$	1026.1	1055.0	476.9	—
	$\text{Ca}K_{\alpha}$	470.6	408.0	145.2	—
	$\text{Fe}K_{\alpha}$	157.8	143.2	83.4	—

(Contains substrate component)

Obviously, the unnormalized results for the particle differ greatly from those for the flat specimen. The normalized results are closer than those obtained at 20 keV, but still can vary by more than 10% relative. The variability in the normalized results is about twice that observed at 20 kV, although some of the results are closer to the flat sample values at 10 kV than at 20 kV. The variability at 10 kV is probably mostly due to the low values of peak-to-background being measured. Statistical fluctuations in the background intensity become much more important as the peak-to-background ratio approaches unity.

---

## 22.3 Irregular or Rough Particles

### *Experiment 22.5: Rastered Beam Analysis Utilizing Particle Shape (Method 3).*

(a) and (b) Processing the example data (see data, Table A22.6) through a conventional correction program and normalizing the results to 100% would produce results similar to those in Table A22.7. (The results are normalized to 99.77% because MnO, which is present in the sample at a level of 0.23 wt%, was not analyzed.) Although the results are better than those obtained in Section 22.2 (in a case where the amount of absorption was considerably greater), they still are not very good. The apparent compositions of magnesium and iron, for example, differ between 10% and 20% from their correct values. For comparison, see the results in the next section.

(c) Correcting for particle ZAF effects dramatically improves the quality of the results. Compare the  $R_{x/Si}$  factors in Table A22.6 to those calculated as a function of particle size in Figures A22.1-A22.3. For example  $R_{Mg/Si}$  for the 12  $\mu\text{m}$  particle was measured to be 1.02 whereas Figure A22.1 gives 1.03. The  $R_{x/Si}$  values indicate how much particle size and shape affect the quantitative analysis. For large flat-topped particles  $R_{x/Si}$  should approach 1. However, small particles and irregularly shaped particles will cause  $R_{x/Si}$  to deviate from 1.  $R_{x/Si}$  values can be used to correct the data for particle and shape effects. Using the sample data and sample geometry (Table A22.6), and the  $R_{x/Si}$  factors given in Figures A22.1-A22.3 for various particle shapes, analyses similar to those of Table A22.8 may be obtained. The calculated compositions of the particles utilizing particle corrections produce results that are almost as good as those obtainable when analyzing thick polished specimens. The differences between measured and actual concentrations are less than 3% relative.

---

**Table A22.7.** Rastered Beam Analyses Uncorrected for Particle Effects

Normalized results	Actual (wt%)	12 $\mu\text{m}$ ptc	4 $\mu\text{m}$ ptc
Mg	9.17	8.77	10.29
Si	25.52	23.99	25.13
Ca	11.02	12.01	10.14
Fe	11.31	13.29	11.47
O	42.75	41.71	42.74
TOTAL	99.77	99.77	99.77

**Table A22.8.** Rastered Beam Analyses Corrected for Particle Effects

Normalized results	Actual (wt%)	12 $\mu\text{m}$ ptc	4 $\mu\text{m}$ ptc
Mg	9.17	9.17	9.40
Si	25.52	25.59	25.24
Ca	11.02	11.04	11.08
Fe	11.31	11.16	11.41
O	42.75	42.81	42.64
TOTAL	99.77	99.77	99.77

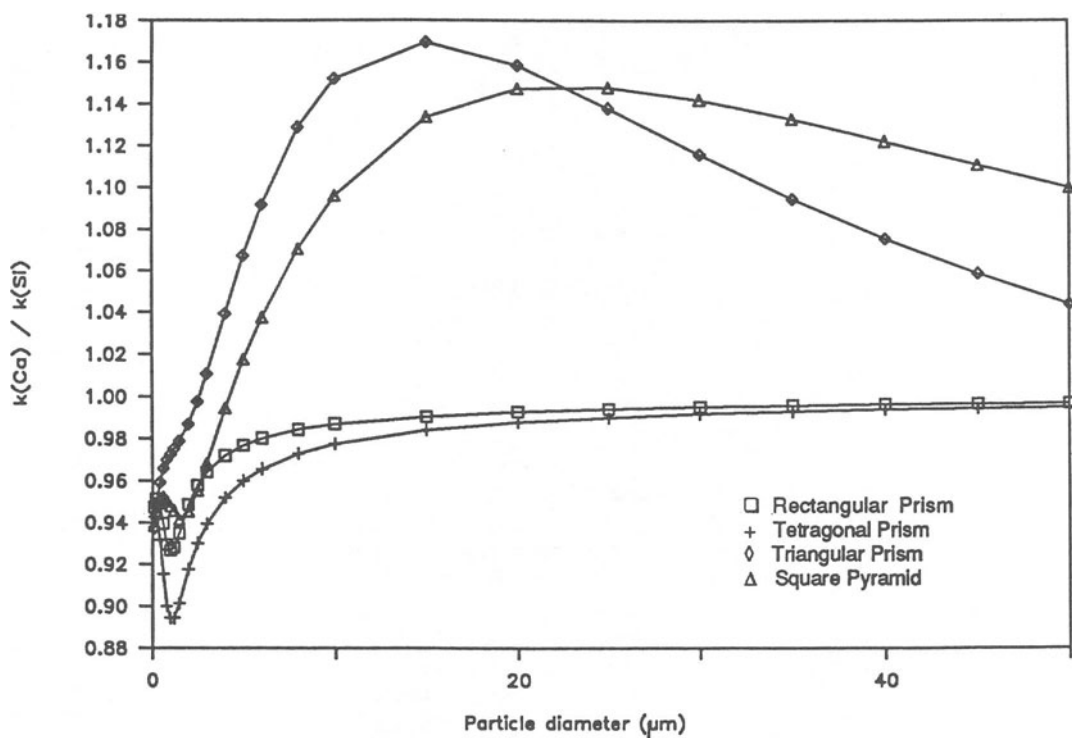


**Figure A22.1.** Relative particle  $K$ -ratios ( $R_{x/\text{Si}}$  factors) for magnesium in NBS K-411 glass particles. 15 kV and 40° take-off angle.

**Table A22.9.** Point Beam Particle Analyses Using Peak-to-Background Ratios

Unnormalized results	Actual (wt%)	4 $\mu\text{m}$ ptc	2 $\mu\text{m}$ ptc
Mg	9.17	6.89	2.94
Si	25.52	26.24	11.86
Ca	11.02	9.55	3.40
Fe	11.31	10.26	5.98
O	42.75	41.18	18.51
TOTAL	99.77	94.12	42.69
Normalized results	Actual (wt%)	4 $\mu\text{m}$ ptc	2 $\mu\text{m}$ ptc
Mg	9.17	7.30	6.87
Si	25.52	27.82	27.71
Ca	11.02	10.12	7.95
Fe	11.31	10.87	13.98
O	42.75	43.65	43.26
TOTAL	99.77	99.77	99.77

---

**Experiment 22.6: Peak-to-Background Ratios (Method 2).** WDS produces better peak-to-background ratios and higher intensities for particles larger than about 1  $\mu\text{m}$ . EDS provides better detection limits for particles smaller than this. Use of WDS requires beam currents of at least 1 nA for reasonable detection limits, while the EDS can be effectively used at currents as low as about 50 pA. A 1-nA electron beam is considerably larger in diameter than a 50-pA SEM beam. Below a minimum critical diameter the beam current required for WDS produces a minimum spot size that is larger than the particle diameter and the detectability becomes worse.

The peak-to-background method can be used to obtain good particle analyses, but it has its limitations, as seen in the example data (Table A22.6). These data, when corrected by conventional techniques, would produce results similar to those of Table A22.9. The results for the 4- $\mu\text{m}$  particle are not too bad, particularly when normalized. With the exception of magnesium, the various elements differ from the actual value by 10% relative or less. However, the results for the 2- $\mu\text{m}$  particle are quite bad. Even the normalized results differ from the correct composition by as much as 25% relative. In both cases, but particularly in the case of the 2- $\mu\text{m}$  particle, part of the measured background radiation probably was produced by electrons interacting with the substrate rather than with the particle. When using massive substrates, the peak-to-background method is limited to analyzing those particles that are significantly larger than the electron range. To analyze  $\mu\text{m}$ -sized or smaller particles using the peak-to-background method, the particles need to be mounted on something like a thin carbon film on a beryllium TEM grid that cannot produce any significant background radiation under electron bombardment.

---

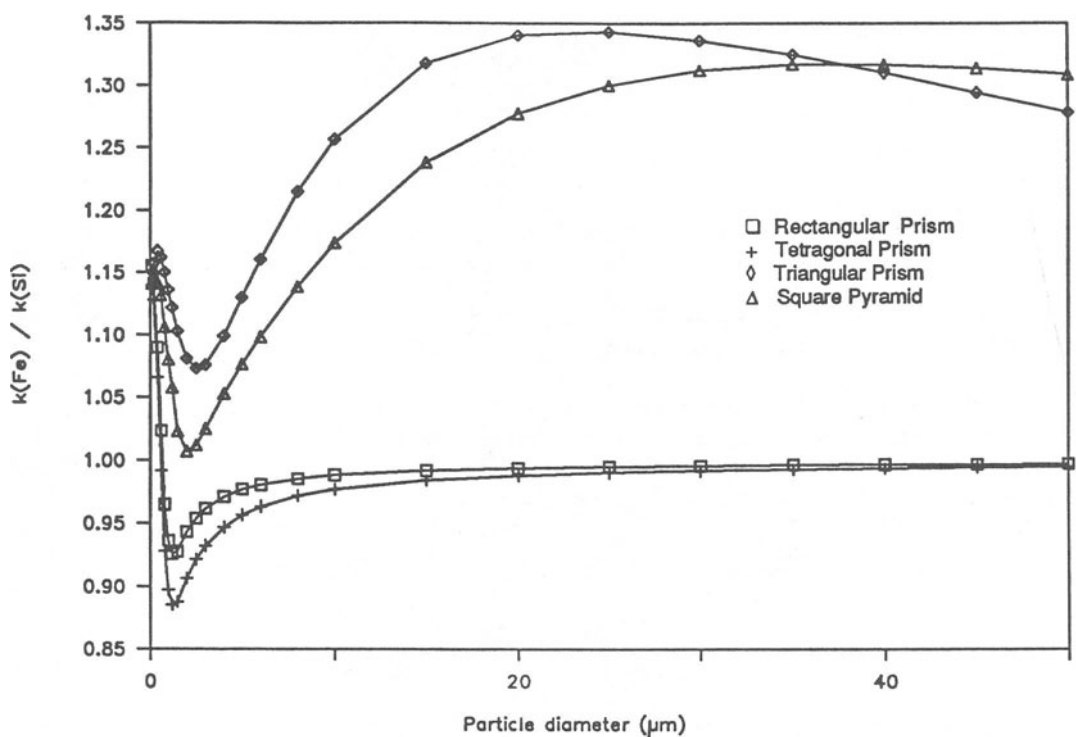


**Figure A22.2.** Relative particle  $K$ -ratios ( $R_{x/Si}$  factors) for calcium in NBS K-411 glass particles. 15 kV and 40° take-off angle.

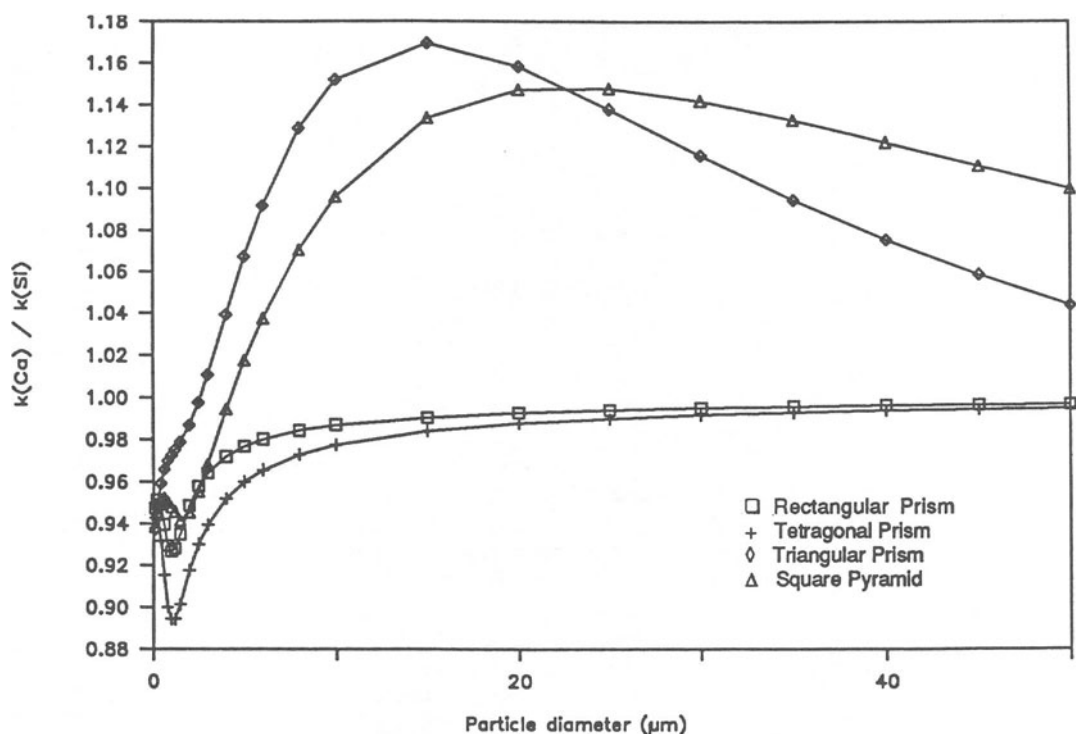


**Figure A22.3.** Relative particle  $K$ -ratios ( $R_{x/Si}$  factors) for iron in NBS K-411 glass particles. 15 kV and 40° take-off angle.

## Laboratory 23

# X-Ray Images

### 23.1 Analog X-Ray Dot Maps

---

**Experiment 23.1: Recording Dot Maps.** (a) Adjustment of CRT recording dot. Various WDS iron x-ray images obtained with different settings of the CRT dot brightness reveal the subjective nature of the analog dot mapping procedure. A dim recording dot (Figure A23.1b) provides a very weak image even where the iron concentration is high and no information at all where the iron concentration is low. The optimum dot brightness image (Figure A23.1c) carries more information but the image is weak and noisy in the iron-poor regions because the total number of x-rays recorded in the 100-sec scan is inadequate to provide the necessary image statistics. Note that both characteristic and bremsstrahlung x-rays of the same energy are recorded since no background correction is applied in the analog WDS scan. The highest intensity dot produces an image (Figure A23.1d) in which the x-ray pulse locations are most easily evident, but the image is not satisfactory because blooming of the dot image causes a loss of resolution and contrast, obscuring fine scale details.

(b) Effect of number of x-ray counts. By increasing the scanning time (and the number of x-ray counts collected) at the optimum dot brightness, the image contrast improves dramatically (Figure A23.1e,f). For the 1000 sec scan (Figure A23.1f) the information content improves in the iron-poor regions but may be lost in the iron-rich regions because the dot density is so great that entire regions are completely white (saturated).

(c) Wavelength-dispersive spectrometer defocusing. The wavelength-dispersive x-ray spectrometer is a focusing device. When the spectrometer is adjusted to be on a characteristic x-ray peak, the focusing criterion is satisfied exactly only for an electron beam generating x-rays on the optic axis of the instrument. The act of scanning the beam to form an image takes the beam away from the optic axis, with the consequence that the collected x-ray intensity falls off. Because the diffraction crystal has a significant width, typically 1 cm, the spectrometer has a line of focus parallel to the crystal width. This focus line is projected as a line of uniform x-ray transmission in the plane of the specimen. At low magnifications (Figure 23.2c), the focus line is visible in the x-ray map and tends to dominate the image contrast, suppressing the true elemental contrast on either side of the line. Figure A23.2d shows a digital EDS image of the same area that exhibits no defocusing. An analog solution to the defocusing problem has been implemented on some instruments. This analog technique effectively adjusts the spectrometer position or the stage z-motion in synchronism with the scan on the specimen to maintain the spectrometer focus line to be coincident with the scan line it progresses through the image frame.

---

### 23.2 Digital X-Ray Images

---

**Experiment 23.2: Choice of Digital Image Parameters.** (a) Given  $\rho = 5.5 \text{ g/cm}^3$ ,  $E_0 = 15 \text{ kev}$ , and  $E_c = 7.1 \text{ keV}$  for iron, the x-ray range is found from Equation 23.1:

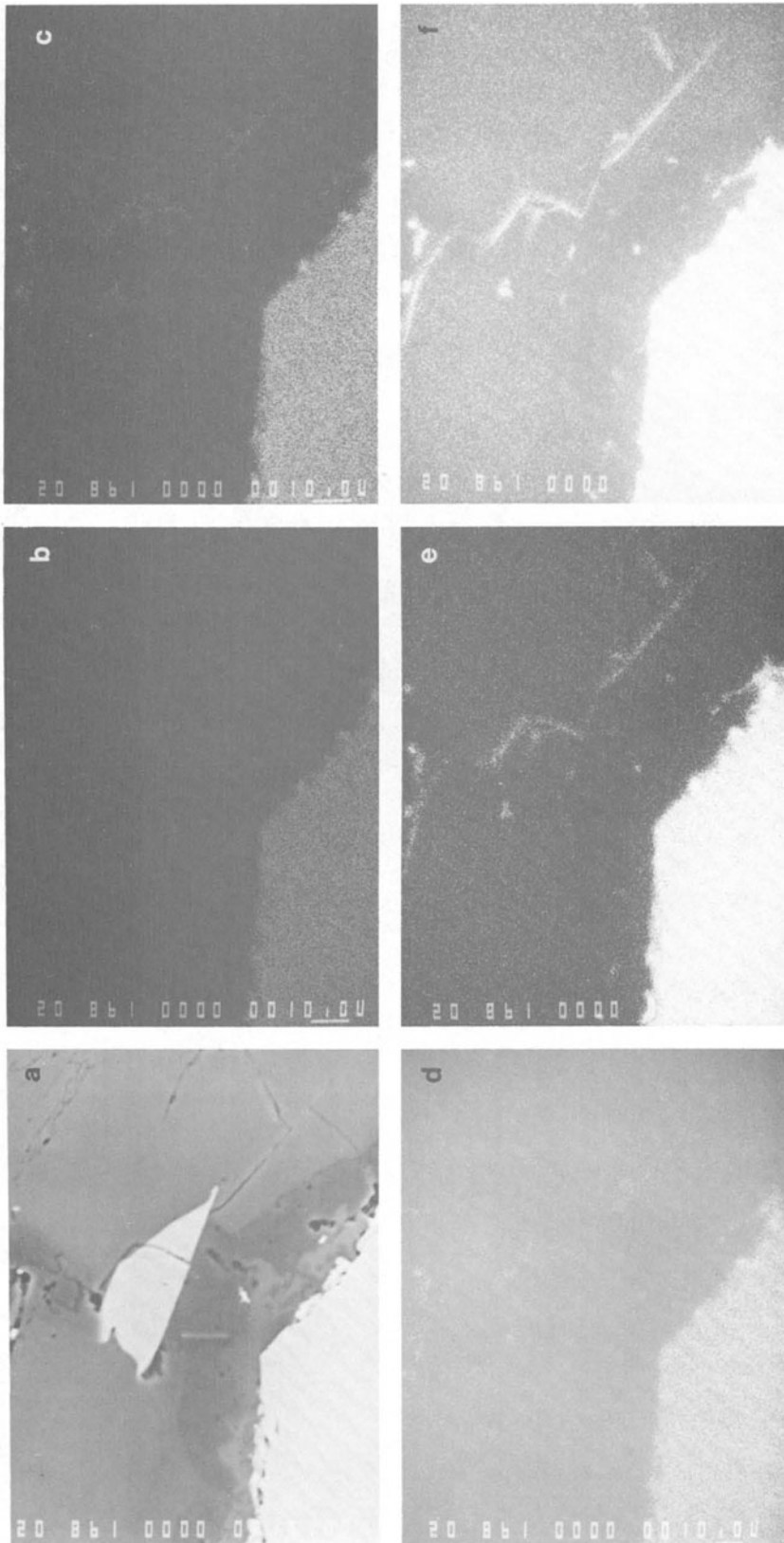


**Figure A23.1.** Wavelength-dispersive WDS  $\text{FeK}_{\alpha}$  images. (a) Secondary electron image of multiphase basalt; (b) analog image dim recording dot (100 sec); (c) optimum recording dot (100 sec); (d) blooming recording dot (100 sec); (e) optimum recording dot (300 sec); (f) optimum recording dot (1000 sec = 16.7 min).

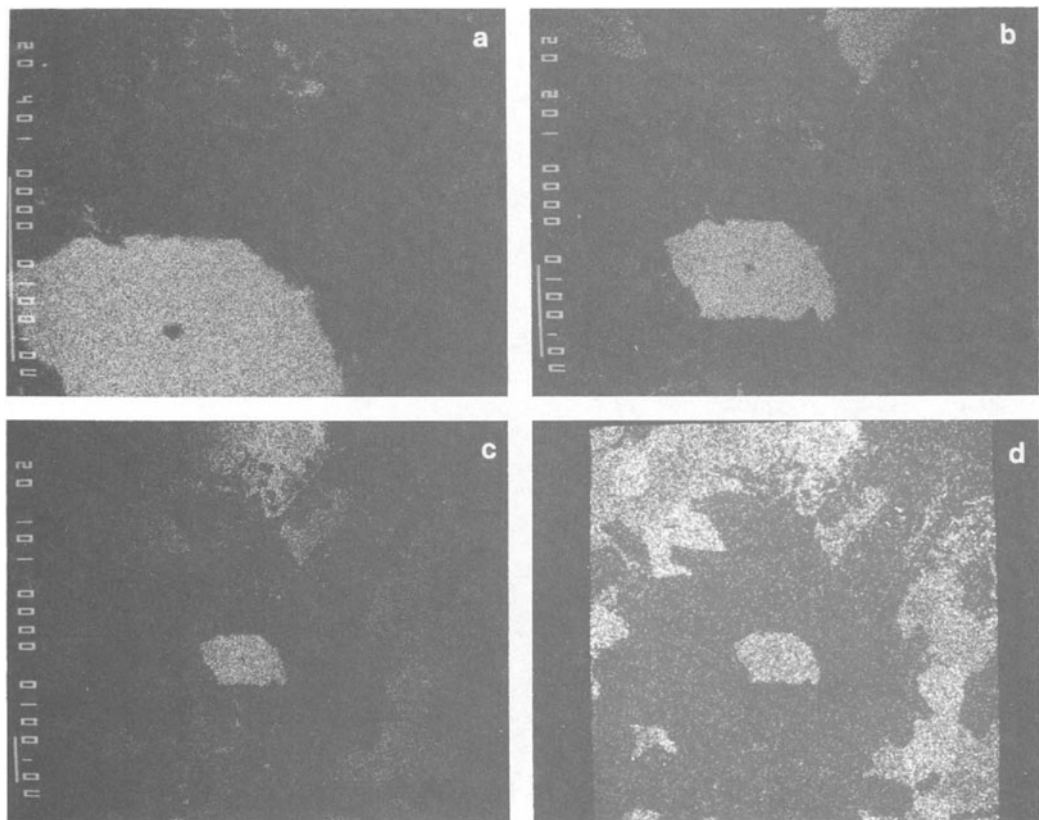


**Figure A23.2.** Wavelength-dispersive spectrometer defocusing. (a) WDS  $\text{Fe}K_{\alpha}$  image at 400x original magnification; (b) WDS  $\text{Fe}K_{\alpha}$  image at 200x original magnification; (c) WDS  $\text{Fe}K_{\alpha}$  image at 100x showing defocusing effects (weaker intensity on the left and right); (d) EDS image of the same area showing no defocusing (even x-ray intensity across the field).

$$\begin{aligned}
 R &= \frac{0.064}{\rho} (E_0^{1.68} - E_c^{1.68}) \mu\text{m} \\
 &= \frac{0.064}{5.5} (15^{1.68} - 7.1^{1.68}) \\
 &= 0.0116 (04.6 - 26.9) = 0.785 \mu\text{m} \\
 R &= 0.79 \mu\text{m}
 \end{aligned}$$

Use Equation 23.2 to find the minimum suitable pixel density where  $L = 100,000 \mu\text{m}$ ,  $M = 860x$ , and  $R = 0.79 \mu\text{m}$ :

$$\begin{aligned}
 n &> \frac{L}{M \cdot R} \\
 n &> \frac{100,000 \mu\text{m}}{860 \times 0.79 \mu\text{m}} = 147
 \end{aligned}$$

**Table A23.1.** Dwell Time Per Pixel

Pixel density	Total number of pixels	Time per pixel ( $t_f = 15$ min)
64 x 64	4096	220 ms
128 x 128	16384	55 ms
256 x 256	65536	14 ms
1024 x 1024	1,048,576	<1 ms

e.g., 147 x 147 pixel density. But the only choices available are 128 x 128 and 256 x 256. In this case, it would be better to raise the magnification to 1000x than to pick 256 x 256 since more counts would be generated.

The final criterion is that the average pixel defining a discrete phase in the x-ray image should have at least 8 counts. The dwell time per pixel for a 15 min frame time can be calculated for all common pixel densities (Table A23.1). Since the average pixel should contain at least 8 counts, this criterion would be more easily met for 128 x 128 than for 256 x 256. If not enough counts per pixel are obtained at either 256 x 256 or 128 x 128, the acquisition time should be increased beyond 15 min. For the examples shown, the pixel density was 128 x 128 and the dwell time per pixel was 55 ms.

(b) To set up the digital scan with an EDS system we must make a window file for the selected elements. Generally, windows are chosen to be slightly larger than full-width-at-half maximum (FWHM) although full-width windows are often used in cases with no overlap. Be sure to set up at least one background window in a region containing no peaks (low-energy side of iron  $K_{\alpha}$  peak). Figure A23.3 shows an EDS spectrum for which the beam was scanned over an area of the basalt in an effort to detect all of the elements present. Elements

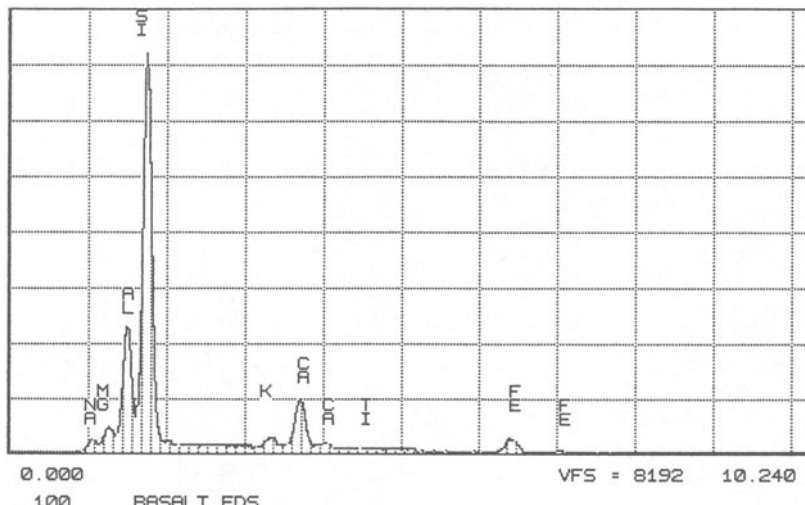


**Figure A23.3.** EDS spectrum of elements detected in basalt. This spectrum is used to determine which elements should be imaged in the digital x-ray image.

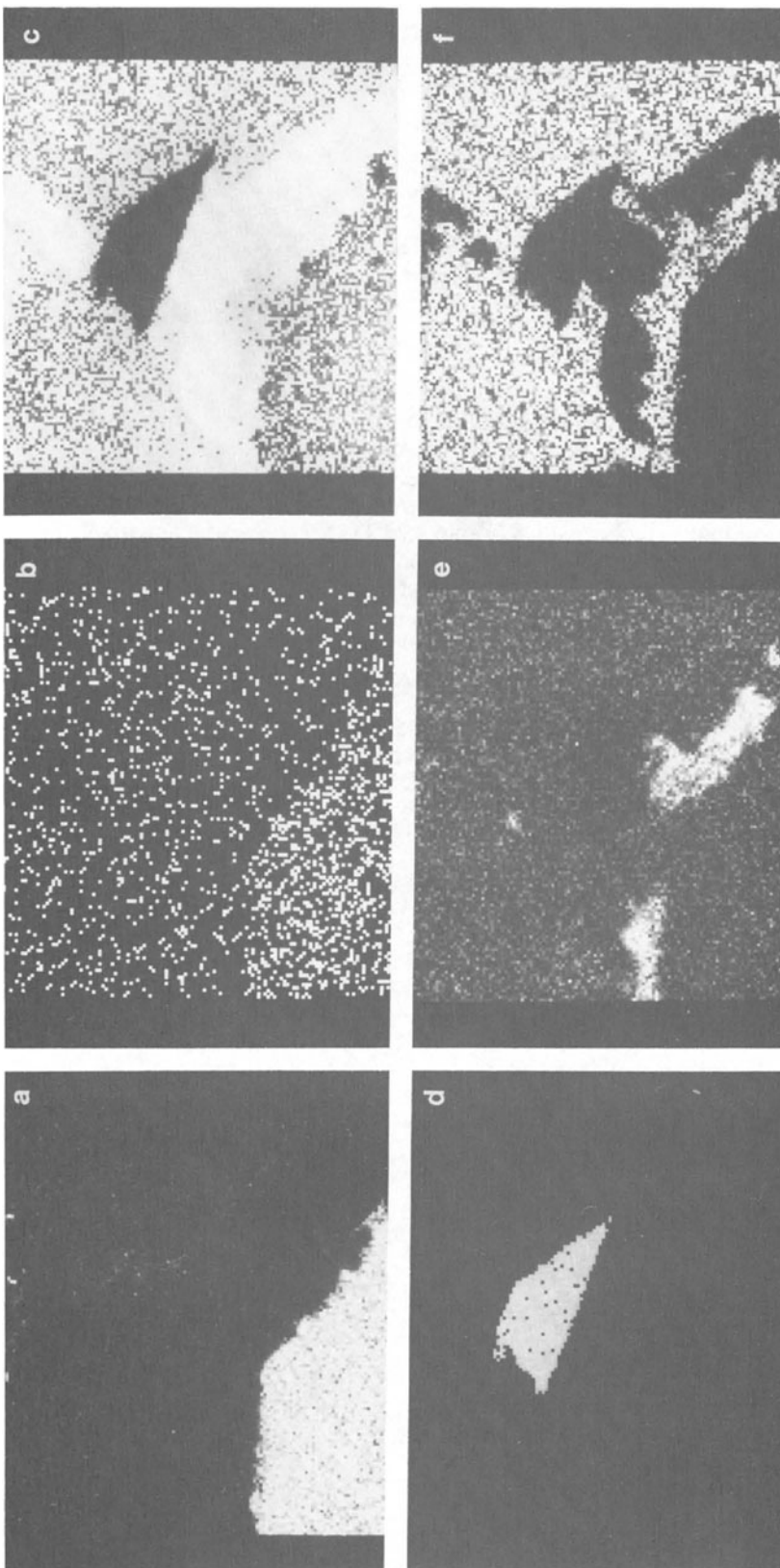


**Figure A23.4.** Digital x-ray images of the same area as Figure A23.1 taken using 128x128 pixels and 55 ms dwell time per pixel. (a) EDS iron image; (b) EDS background image; (c) EDS silicon image; (d) EDS calcium image; (e) EDS potassium image; (f) EDS aluminum image.

detected were sodium, magnesium, aluminum, silicon, potassium, calcium, titanium, and iron. The parameters selected in Experiment 23.2a produced the EDS digital x-ray images shown in Figure A23.4. While these images are not background-subtracted, they provide a good indication of the location of each element. However, the iron EDS image (Figure A23.4a) does not reveal the distribution of iron in the iron-poor regions as well as the analog WDS dot map iron image (Figure A23.1e,f) for which the peak-to-background is about 10 times greater.

(c) The WDS system will easily produce more than 8 counts per pixel in the iron-containing phase. Figure A23.5b shows the WDS digital iron image, which exhibits an even better signal-to-background ratio than the analog dot map (Figure A23.1e,f) because relative intensity values are displayed. The estimated average counts per pixel in the iron-rich phase (white) is about 800 in Figure A23.5b. In the regions of lower iron concentration near the middle of the frame the range is from 8 to 170 counts per pixel.

---

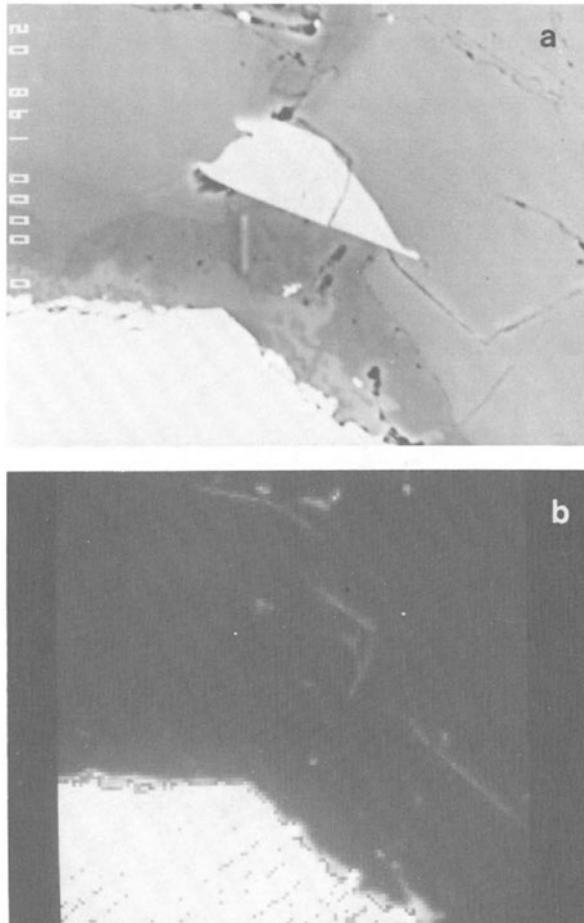


**Figure A23.5.** WDS digital x-ray image. (a) SE image; (b) WDS  $\text{Fe}K_{\alpha}$  image using 128x128 pixels and 55 ms dwell time per pixel.

## 23.3 Background Removal

---

**Experiment 23.3: Background Subtraction.** Background may either be subtracted on-the-fly for each pixel before the counts for that pixel are stored or subtracted after the element image is acquired by subtracting an image collected with a nearby background window. Figure A23.6 shows results from on-the-fly background subtraction for silicon, titanium, and iron. The chromium and background images (Figures A23.6e,f) appear similar. Both images show a slight enhancement of background signal in the area of high iron concentration. The background image is a good check to see if an element is really present. If present an element should show an x-ray image with contrast stronger than the background image.

---

## 23.4 Dead Time Considerations

---

**Experiment 23.4: Test of the Dead Time Circuit.** Early digital imaging systems employing EDS detectors did not correct for dead time variations across the image. Thus, when a region of the specimen was encountered containing a very high concentration of an element, the counting rate increased until the dead time reached 100% which effectively shut off the detector. This produced the annoying situation in which a round region of pure copper would be imaged as a copper ring rather than a filled circle. One remedy for this problem is to use a shorter time constant on the detector amplifier. Another solution is to extend the live time to compensate for the effect. However, even this correction may not be accurate, and the test described in this experiment is a check of this circuit.

- (a) At 5% dead time the EDS iron image (Figure A23.7) should look similar to the digital WDS image (Figure A23.5b) in that it should reveal both high and low iron concentrations. In this case, a count rate yielding 5% dead time produced an image with too few iron counts. In order for this experiment to be statistically meaningful, the counting time should be extended to 1000 sec. Figure A23.7b shows an iron image taken at 20% dead time. This EDS image is similar to the WDS image (Figure A23.5b) except that there are still too few counts collected.
- (b) At 50% dead time the iron image has more counts per pixel but it shows much less detail and has a blurred appearance (Figure A23.7c).
- (c) The ratios of iron counts in the same pixels for the high- and low-iron regions at each dead time are shown in the following table:

---

Region	5% dead time	20% dead time	50% dead time
High iron	1	11	59
Low iron	0	5	8

---

Clearly, in this case the differences in iron count ratios are more likely due to insufficient counts in the pixels rather than an error in the dead time circuit. To establish that a problem exists in the dead time circuit more counts in each iron-containing phase should be taken.

---

## 23.5 Intensity Measurement

---

**Experiment 23.5: X-Ray Line Scans.** The x-ray line scan is useful for quantitative analysis since relative changes in concentration along a line in the image can be accurately

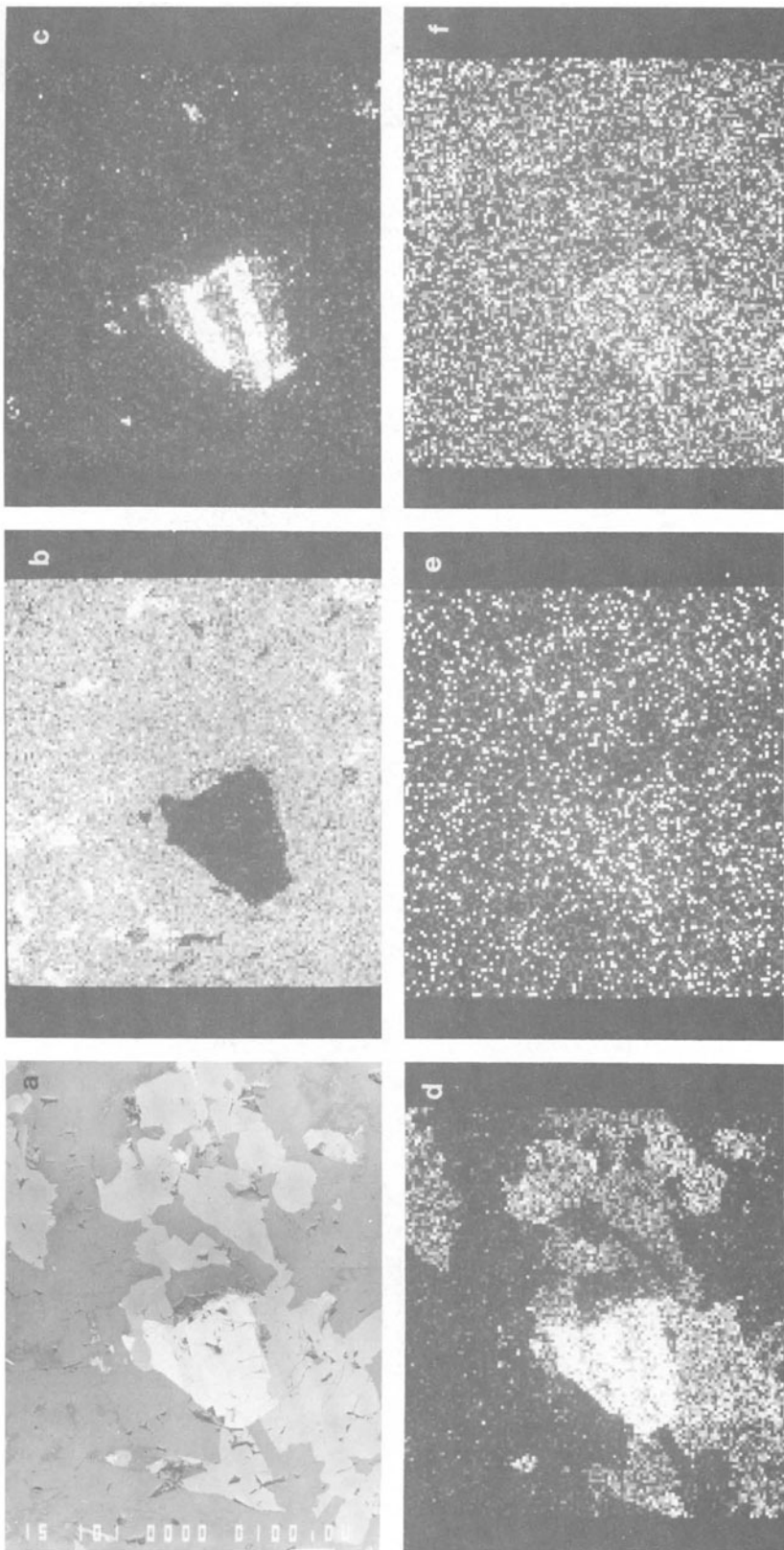


**Figure A23.6.** EDS x-ray images with background subtraction. (a) Secondary electron image of basalt; (b) silicon image; (c) titanium image; (d) iron image; (e) chromium image; (f) background image from a region of interest of lower energy than chromium. Background was subtracted on-the-fly for images (b)-(d).

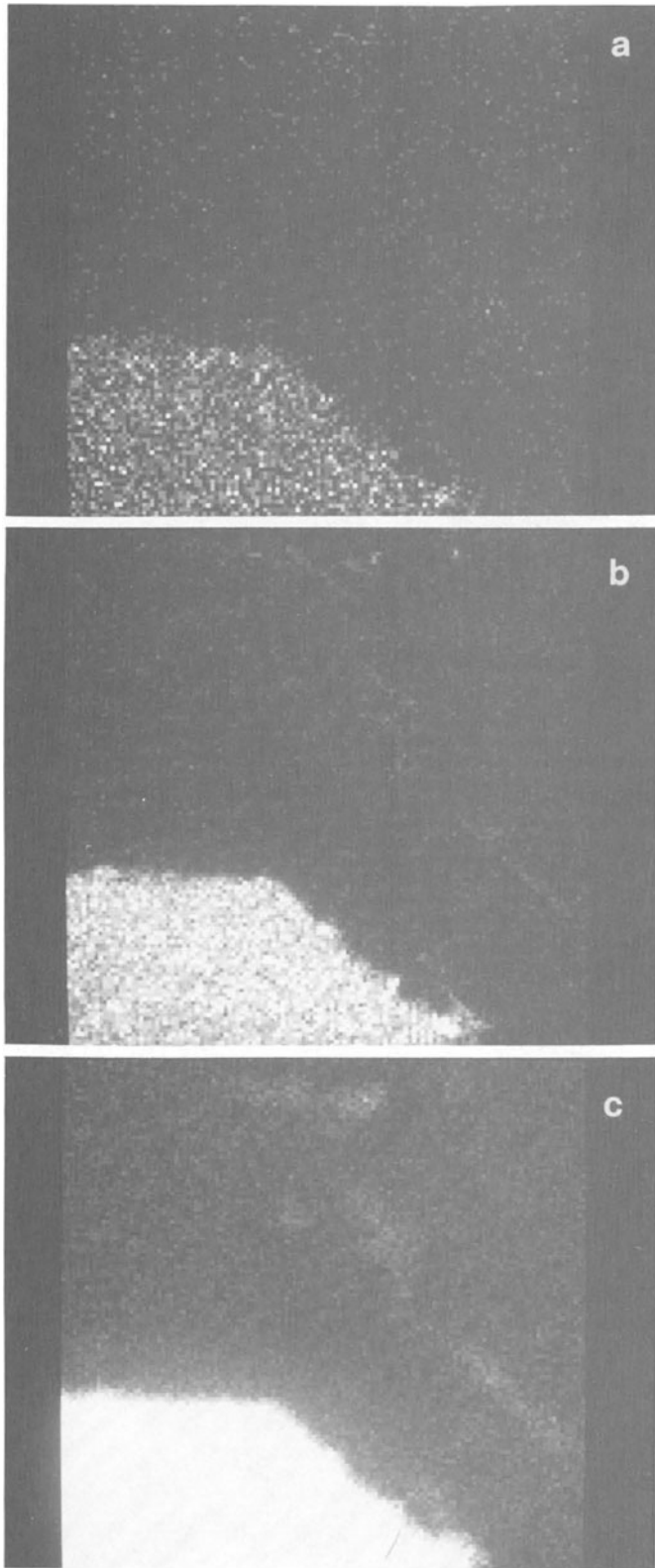


**Figure A23.7.** Effect of counting rate. (a) Iron image taken with 5% dead time; (b) iron image taken with 50% dead time; (c) iron image taken with 50% dead time.

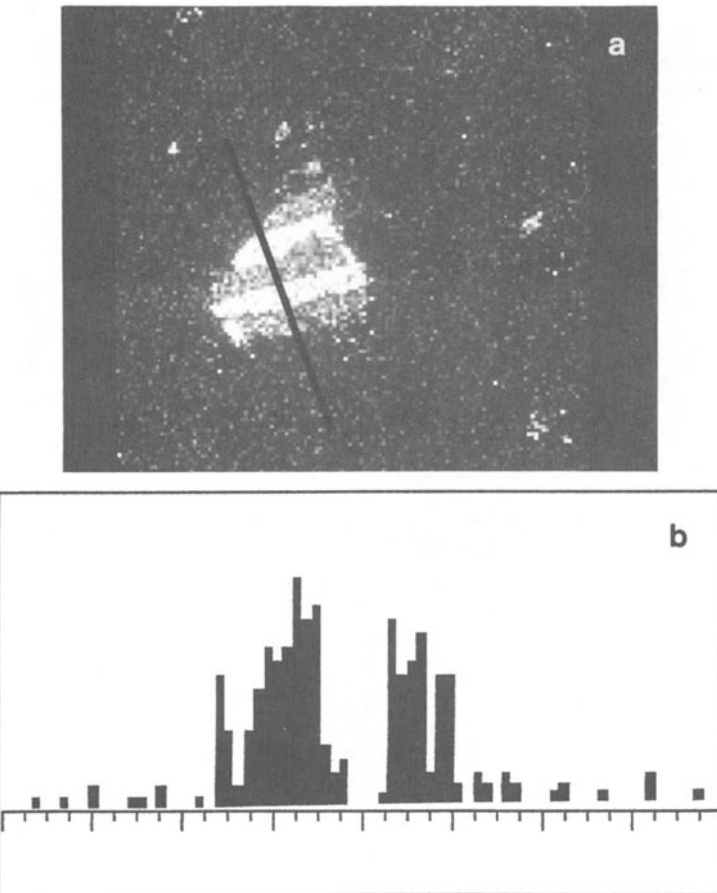


**Figure A23.8.** Line scan across a titanium region of basalt. (a) EDS titanium image from Figure A23.6; (b) titanium line scan.

determined without the nonlinear effects of human vision. Figure A23.8 shows a line scan across a portion of the titanium image from Figure A23.6. Line scans are especially important when there are not enough counts in a full range image to show a smooth variation in concentration. If the time devoted to a 128x128 digital image were used just to collect a digital line scan, the counts per pixel should increase by two orders of magnitude.

## 23.6 X-Ray Image Processing

---

**Experiment 23.6: Image Smoothing.** Image smoothing can be of great benefit for x-ray images particularly those collected with few counts. However, worm-like artifacts can appear after smoothing with a kernel that is too small. See the solution to Experiment 17.7 for examples of this.

---

**Experiment 23.7: Primary Coloring.** Color coding three elements with the primary colors allows different phases to be imaged clearly. For example, adding the red silicon image (Figure A23.4c) to the green potassium image (Figure A23.4e) clearly shows the regions

containing both elements in yellow. For another example, combine a red iron image (Figure A23.6d) with a green titanium image (Figure A23.6c) and a blue silicon image (Figure A23.6b). Other examples are shown in *ADSEMXM*, Chapter 5, Figures 5.17A-D.

---